

A HIGH-OUTPUT, SIZE-SELECTIVE AEROSOL GENERATOR

By

HUNGMIN CHEIN

A DISSERTATION PRESENTED TO THE GRADUATE SCHOOL  
OF THE UNIVERSITY OF FLORIDA IN PARTIAL FULFILLMENT  
OF THE REQUIREMENTS FOR THE DEGREE OF  
DOCTOR OF PHILOSOPHY

UNIVERSITY OF FLORIDA

1994

## ACKNOWLEDGMENTS

First and foremost, I would like to express sincere appreciations to my advisor, Dr. D. A. Lundgren. Dr. Lundgren's guidance and encouragement throughout the course of this work have contributed greatly to its success. My graduate studies could not have been so enjoyable and fruitful without his generous support.

This work was conducted as part of a subcontract with Alliance Technologies Corporation, the prime contractor on EPA 68-D0-0114 (Environmental Exposure System and Ancillary Facilities). The assistance of Dr. Jon Berntsen, the project engineer, is gratefully acknowledged.

I would like to thank Mr. Ken Reed for his assistance in machining the improved virtual impactor. His expertise is gratefully appreciated.

I would also like to thank Dr. E. R. Allen, Dr. P. A. Chadik, Dr. C. Hsu, and Dr. R. Mei for their time and effort required to serve as my doctoral committee members. Each member, in his own way, has served as a source of inspiration during the course of my studies at the University of Florida.

Finally, I would like to thank my wife, Ma-Li, for her patience and encouragement during the last five years. Especially, I like to thank her for taking good care of our daughter, Karen, during the last two years so that I can complete this work successfully.

## TABLE OF CONTENTS

ACKNOWLEDGMENTS .....	ii
LIST OF TABLES .....	v
LIST OF FIGURES .....	vi
KEY TO SYMBOLS .....	ix
ABSTRACT .....	xii
CHAPTER 1	
INTRODUCTION .....	1
Atomization .....	1
Particle Deposition in the Human Respiratory Tract .....	3
Characteristics of Test Aerosols .....	8
EPA Human Exposure Laboratory .....	9
Project Objectives .....	11
Project Accomplishments .....	14
CHAPTER 2	
REVIEW OF LITERATURE .....	16
Background .....	16
Conventional Virtual Impactors .....	17
Multi-Stage and Parallel-Stage Virtual Impactors .....	19
Virtual Impactors with Central Clean Air Cores .....	20
Turbulent-Flow and Counterflow Virtual Impactors .....	21
Applications .....	22
CHAPTER 3	
MATERIALS AND METHODS .....	24
Description of the Aerosol Generator .....	24
Improved Virtual Impactors .....	27
Aerodynamic Particle Sizer .....	38
Experimental Procedure .....	44

CHAPTER 4	RESULTS AND DISCUSSION	51
	Testing of Delavan Simplex Nozzles	51
	Performance of the High-Output, Size-Selective Aerosol Generator	60
CHAPTER 5	CONCLUSIONS	93
	Testing of Delavan Simplex Nozzles	93
	Performance of the High-Output, Size-Selective Aerosol Generator	94
APPENDIX		
	DETAILED DESIGN DRAWINGS OF THE GENERATION CHAMBER, THE IMPROVED VIRTUAL IMPACTOR, AND THE CLEAN AIR SECTION.	97
REFERENCE LIST		111
BIOGRAPHICAL SKETCH		114

## LIST OF TABLES

<u>Table</u>	<u>page</u>
1-1. Aerosols needed in EPA human exposure chamber.....	10
3-1. Geometric dimensions of the improved virtual impactor set I and II ( $W_c=22.0$ mm, $A_1=30^\circ$ , $A_2=15^\circ$ , $A_3=30^\circ$ , $A_4=45^\circ$ , and $A_5=15^\circ$ ).....	34
4-1. MMAD, GSD, and Ma of three data sets used to evaluate the system stability and repeatability.....	70
4-2. Two sets of basic operating conditions and the aerosol outputs using a 9% sodium chloride solution (the Delavan spray nozzle was operated at $P_A=207$ kPa and $P_L=-40$ cm of water).....	79

## LIST OF FIGURES

<u>Figure</u>	<u>page</u>
1-1. The human respiratory system.....	4
1-2. Total deposition in human respiratory tract.....	7
1-3. Schematic diagram of a solid-cone simplex nozzle.....	12
1-4. Schematic diagram of virtual impactors.....	13
3-1. Schematic diagram of the high-output, size-selective aerosol generator.....	24
3-2. An assembly view of the aerosol generation chamber.....	25
3-3. Schematic diagram of the aerosol flow with the central air core in the acceleration nozzle.....	27
3-4. Schematic diagram of the improved virtual impactor.....	31
3-5. Schematic diagram of the clean air section.....	33
3-6. Photograph of the virtual impactor with the clean air tube.....	35
3-7. Schematic diagram of the aerodynamic particle sizer.....	37
3-8. Experimental set-up used to test the Delavan simplex nozzles.....	44
3-9. Experimental set-up used to evaluate the performance of the high-output, size-selective aerosol generator.....	46
3-10. Photograph of the evaluation system showing the prototype aerosol generator.....	48
4-1. Liquid flow rate and nebulizing air flow rate as a function of atomization pressure for the Delavan simplex nozzle #30609-2.....	50

4-2. Aerosol generation rate as a function of atomization pressure for the Delavan simplex nozzle #30609-2.....	51
4-3. Particle mass concentration histograms generated by the simplex nozzle #30609-2 at different atomization pressures, $P_A$ . The dotted point shows the log-normal fitting curve. a) $P_A = 69$ kPa; b) $P_A = 138$ kPa.....	53
4-4. Particle mass concentration histograms generated by the simplex nozzle #30609-2 at different atomization pressures, $P_A$ . The dotted point shows the log-normal fitting curve. a) $P_A = 207$ kPa; b) $P_A = 276$ kPa.....	54
4-5. Aerosol generation rate as a function of liquid pressure for the Delavan simplex nozzle #30609-2 combined with #30610-1.....	56
4-6. Aerosol generation rate as a function of atomization pressure for the Delavan simplex nozzle #30609-5.....	57
4-7. Liquid flow rate and aerosol generation rate as a function of liquid pressure for the Delavan simplex nozzle #30609-5.....	59
4-8. Particle size distributions produced by the simplex nozzle #30609-5 at the optimum condition ( $P_A = 207$ kPa and $P_L = 40$ cm of water). a) Mass histogram; b) Mass cumulative curve.....	60
4-9. Particle concentration histograms generated by the aerosol generator with virtual impactor $W = 10$ mm (no fine particle contamination). a) Number histogram; b) Mass histogram.....	62
4-10. Particle concentration histograms generated by the aerosol generator with virtual impactor $W = 15$ mm (no fine particle contamination). a) Number histogram; b) Mass histogram.....	63
4-11. Particle concentration histograms generated by the aerosol generator with virtual impactor $W = 15$ mm (with fine particle contamination). a) Number histogram; b) Mass histogram.....	65
4-12. Particle concentration histograms generated by the aerosol generator with virtual impactor $W = 10$ mm (with fine particle contamination). a) Number histogram; b) Mass histogram.....	66
4-13. Particle size distributions measured by the APS. a) With the TSI dilutor; b) Without the TSI dilutor.....	68

4-14. Shape change of particle mass concentration histograms due to the variation of particle count, $N_p$ . a) $N_p=181$ ; b) $N_p=781$ .	72
4-15. Shape change of particle mass concentration histograms due to the variation of particle count, $N_p$ . a) $N_p=1251$ ; b) $N_p=4622$ .	73
4-16. Particle mass concentration histograms obtained with different clean air tube distances, $Sc$ (tube diameter, $W_c$ , = 14 mm). a) $Sc=10$ mm; b) $Sc=20$ mm.	75
4-17. Particle mass concentration histograms obtained with different clean air tube distances, $Sc$ (tube diameter, $W_c$ , = 14 mm). a) $Sc=40$ mm; b) $Sc=60$ mm.	76
4-18. Particle concentration histograms obtained with the clean air tube distance, $Sc$ , and tube diameter, $W_c$ , of 45 mm and 22 mm, respectively. a) Number histogram; b) Mass histogram.	77
4-19. Particle mass concentration distributions using 9% sodium chloride solution at operating condition set #1. a) Mass histogram; b) Mass cumulative curve.	80
4-20. Particle mass concentration distributions using 9% sodium chloride solution at operating set #2. a) Mass histogram; b) Mass cumulative curve.	83
4-21. Particle mass concentration distributions using 1% sodium chloride solution at operating condition set #1. a) Mass histogram; b) Mass cumulative curve.	85
4-22. Particle mass concentration distributions using 0.05% sodium chloride solution at operating condition set #1. a) Mass histogram; b) Mass cumulative curve.	86
4-23. Salt concentration and number of generators as a function of particle aerodynamic diameter based on operating condition set #1 (solid line for theoretical calculation and circle points for experimental data).	88
4-24. Particle mass concentration distributions obtained with operating condition set #2 but minor flow rate=4.3 lpm. a) Mass histogram; b) Mass cumulative curve.	89



## KEY TO SYMBOLS

$C$  = particle Cunningham correction factor

$C_{ae}$  = Cunningham correction factor for aerodynamic diameter

$C_e$  = Cunningham correction factor for equivalent volume diameter

$d$  = particle diameter

$d_{50}$  = impactor cutoff aerodynamic diameter

$d_{ae}$  = particle aerodynamic diameter

$d_{APS}$  = particle aerodynamic diameter measured by APS

$d_d$  = droplet diameter

$d_w$  = equivalent volume diameter of solid particle

GSD = geometric standard deviation

$M$  = aerosol mass concentration

$Ma$  = aerosol generation rate

MMAD = mass median aerodynamic diameter

M.W. = molecular weight of the air (0.0289 Kg/mole).

$N$  = aerosol number concentration

NMAD = number median aerodynamic diameter

$N_p$  = particle count

$P$  = upstream (ambient) pressure

$\Delta P$  = pressure drop between the sampling inlet and the detection tube.

$P_A$  = atomization air pressure

$P_L$  = liquid pressure

$Q_a$  = minor flow rate of the improved virtual impactor

$Q_c$  = clean air flow rate of the improved virtual impactor

$Q_l$  = liquid flow rate

$Q_n$  = nebulizing air flow rate

$Q_t$  = total flow rate of the improved virtual impactor

$Q_w$  = major flow rate of the improved virtual impactor

$R$  = gas constant (8.31 J/K-mole)

$Re$  = Reynolds number

$r_1$  = radius of the central clean air flow

$r_2$  = impactor nozzle radius

$r_c$  = critical radius within which the accelerated particles are separated from the major flow and pass into the minor flow.

$Sc$  = clean air tube distance

$Stk$  = Stokes number

$T$  = temperature ( $^{\circ}K$ )

$t$  = time interval associated with particle acceleration

$U$  = particle velocity relative to air velocity

$V_g$  = centerline air velocity

$V_0$  = average fluid velocity at impactor nozzle exit

$W$  = impactor nozzle diameter

$W_c$  = clean air tube diameter

$\gamma$  = minor flow ratio (=  $Q_a / Q_t$ )

$\eta$  = separation efficiency of an improved virtual impactor

$\eta_0$  = separation efficiency of a conventional virtual impactor

$\lambda$  = gas mean free path

$\mu$  = air dynamic viscosity

$\rho_0$  = reference particle density of 1000 kg/m<sup>3</sup>

$\rho_a$  = air density

$\rho_p$  = particle density

$\rho_c$  = calibrant particle density

$\tau$  = particle relaxation time

$\chi$  = particle dynamic shape factor

$\chi_c$  = dynamic shape factor of calibrant particles

$\omega$  = clean air flow ratio (=  $Q_c / Q_t$ )

Abstract of Dissertation Presented to the Graduate School  
of the University of Florida in Partial Fulfillment of the  
Requirements for the Degree of Doctor of Philosophy

A HIGH-OUTPUT, SIZE-SELECTIVE AEROSOL GENERATOR

By

HungMin Chin

August 1994

Chairperson: Dale A. Lundgren

Major Department: Environmental Engineering Sciences

An aerosol generator capable of generating a narrow size-distribution aerosol with high mass concentrations was designed, fabricated, and tested. Gravity was used to remove large particles and a virtual impactor was employed to remove small particles. Aerosols generated from a sodium chloride solution (0.05% to 9% by volume) were found to have a mass median aerodynamic diameter (MMAD) in the range of 1.38 to 9.99  $\mu\text{m}$  and a geometric standard deviation (GSD) varying from 1.18 to 1.46. Aerosol generation rate (Ma) varied from 0.21 to 23.8 mg/min depending upon the particle size produced. The overall dimensions of this generator were about 190 cm in height and 15 cm in diameter.

Droplet generation was performed with a Delavan simplex nozzle. Three combinations of simplex nozzles were tested. The Delavan simplex nozzle #30609-5 installed on the bottom of the 15 cm diameter generation chamber was found to be most

suitable. The selected operating conditions were: atomization pressure = 207 kPa and liquid pressure = -40 cm of water (-3.9 kPa relative to the ambient pressure). At these operating conditions, the nebulizing air flow rate was 47 lpm and the liquid flow rate was 36 ml/min. The MMAD, GSD, and Ma of the generated liquid aerosol (leaving the generation chamber) were about 4  $\mu\text{m}$ , 2, and 0.6 g/min, respectively.

Liquid droplets were segregated by an improved virtual impactor with a clean air core and evaporated to form solid particles with narrow size distributions. Two sets of acceleration nozzles and collection probes were interchangeably employed in the virtual impactor. The virtual impactor was demonstrated to segregate droplets very efficiently and the generated aerosol had a nearly perfect log-normal distribution. Based on the number distribution, the MMAD values obtained by using the Hatch-Choate equation and by log-normal fitting of the converted mass distribution agreed extremely well. The virtual impactor set I was operated at aerosol flow rate ( $Q_n$ ) = 47 lpm, clean air flow rate ( $Q_c$ ) = 15 lpm, and minor flow rate ( $Q_a$ ) = 8 lpm, while set II was operated at  $Q_n$ =47 lpm,  $Q_c$ =27 lpm, and  $Q_a$ =14 lpm. The liquid aerosol selected by virtual impactor set I was calculated to have a MMAD of 9.73  $\mu\text{m}$ , GSD of 1.29, and Ma of 120 mg/min, while the liquid aerosol selected by set II had a MMAD of 12.8  $\mu\text{m}$ , GSD of 1.24, and Ma of 71 mg/min.

## CHAPTER 1 INTRODUCTION

### Atomization

The process of atomization is one in which a liquid jet or sheet is disintegrated by the kinetic energy of the liquid itself, or by exposure to high-velocity air or gas, or as a result of mechanical energy applied externally through a rotating or vibrating device (Lefebvre, 1989). Atomization is of importance in several industrial processes and has many other applications in agriculture, meteorology, and medicine.

### Classification of Atomizers

Atomization results from an energy source acting on bulk liquid. There are three major kinds of atomizers employing different types of energy to transform the bulk liquid into sprays. Their characteristics are briefly discussed below.

Pressure atomizers. As a liquid is discharged through a small orifice under high applied pressure, the pressure energy is converted into kinetic energy. The kinetic energy is utilized to break up the liquid film and produces a wide range of drop sizes. A basic pressure atomizer is a plain orifice atomizer which employs a simple circular orifice to inject a round jet of liquid into the surrounding air. Small orifices are able to achieve fine atomization but orifice plugging problems limit the minimum orifice size to around

0.3 mm. Another kind of pressure atomizer is a pressure-swirl or simplex atomizer. A swirling motion is imparted to the liquid by forcing the air or liquid through tangential holes or slots in the atomizer. Atomization efficiencies of simplex atomizers are generally good.

Rotary atomizers. In rotary atomization, the feed liquid is centrifugally accelerated to a high velocity before being discharged into the surrounding air. The liquid is distributed centrally on the disk or cup. The liquid flows radially outward across the disk and is discharged at high speed from its periphery. At low flow rates, droplets form near the edge of the disk. At high flow rates, ligaments or sheets are generated at the edge and disintegrate into droplets. Rotary atomizers allow independent variation of flow rate and disk speed and, therefore, provide more flexibility in operation.

Pneumatic atomizers. Pneumatic or two-fluid nozzle atomization involves impacting liquid bulk with high-velocity gas. The mechanism of atomization is one of high-velocity gas creating high frictional forces over liquid surfaces causing liquid disintegration into spray droplets (Masters, 1985). Sprays are characterized by high homogeneity. However, it is difficult for high-velocity air to penetrate the thick solid liquid jets at larger liquid feed rates. Therefore, atomization is incomplete and there is a wide droplet-size distribution throughout the resulting spray.

### Spray Patterns

A conical or flat spray pattern may be generated to achieve the desired dispersion of drops for liquid-gas mixing. Conical sheets may be produced by pressure-swirl nozzles

in which tangential holes or slots are employed to impart a swirling motion to the liquid as it exits the nozzle. Flat sheets are generally produced either by forcing the liquid through a narrow annulus or by feeding it to the center of a rotating disk or cup. Regardless of how the sheet is developed, its initial hydrodynamic instabilities are enlarged by aerodynamic disturbances and it produces a wide range of drop sizes. The average drop diameter is dependent mainly on the initial thickness of the liquid sheet, its velocity relative to the surrounding gas, and the liquid properties of viscosity and surface tension.

#### Particle Deposition in the Human Respiratory Tract

Particle size, concentration, and composition play an important role in the assessment of the health hazards associated with inhalation of atmospheric particles. The location of aerosol deposition in the respiratory tract of the human body is dependent on particle size. The quantity of deposition is directly proportional to the mass concentration. The composition of the aerosol determines both efficiency and mechanism of particulate removal. Figure 1-1 shows the various components of the human respiratory system which can be grouped into three major sections. The head region consists of the nose, mouth, pharynx, and larynx. The airways from the larynx to the terminal bronchiole compose the tracheobronchial region. The location of gas-exchange is referred to as the pulmonary or the alveolar region.



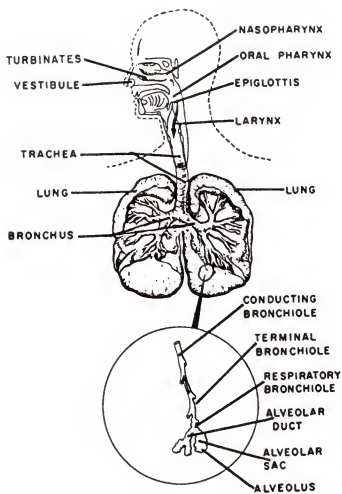


Figure 1-1. The human respiratory system. Source: Hinds, 1982, pg. 212.

### Deposition Mechanisms

A simplistic discussion of particle inhalation physics neglecting anatomical variations, discrepancies in tidal volume, and other nonideal considerations is presented below. There are five pathways by which airborne particles may deposit: impaction, sedimentation, diffusion, interception, and electrostatic precipitation.

Impaction. Sharp bends and relatively high velocities make inertial impaction the primary mechanism of deposition in the head region and the upper tracheobronchial region. Due to their inertia, large particles deviate from the airflow streamline at bends and impact on the wall of the bend in the nasal passages and tracheobronchial bifurcations. This is the dominant removal mechanism for a majority of the mass associated with atmospheric aerosols.

Sedimentation. Suspended particles able to escape collection by inertial impaction will encounter the low velocity and small-diameter airways of the smaller bronchi, bronchiole, and alveolar region. These conditions are ideal for particle deposition due to gravitational sedimentation.

Diffusion. The high velocity of air molecules imparts random Brownian motion to airborne particles, particularly those less than 0.5  $\mu\text{m}$  in size. Efficiency of removal by this mechanism is inversely proportional to particle size and is increased in smaller airways where distances are short and residence time is long (the pulmonary region).

Interception. Interception occurs when the trajectory of a particle brings it sufficiently close to an object so that its physical size causes it to intercept the object and,

hence, be deposited. Removal by interception can occur for all particles, but it is most important for long fibrous particles having small inertia but large physical size.

Electrostatic precipitation. The charge associated with an aerosol may promote collection by electrostatic precipitation. Unipolar charged particles will be forced to the walls of airways due to their mutual repulsion. Furthermore, deposition may result from image charges induced on the surface of the airways by charged particles. This mechanism is of least concern due to the fact that atmospheric aerosols usually have a low electrical charge.

### Total Deposition

Experimental measurements of total deposition, the combined deposition of particles in all regions of the respiratory system, have been performed by measuring the concentration of inhaled and exhaled monodisperse test aerosols under controlled conditions. Figure 1-2 shows the experimental data of total deposition as a function of aerodynamic diameter ( $d_{ae}$ ), except below  $0.5\ \mu\text{m}$ , where geometric diameter is used. The aerodynamic diameter,  $d_{ae}$ , is the diameter of the unit density ( $\rho_p=1\ \text{g/cm}^3$ ) sphere that has the same settling velocity as the particle (Hinds, 1982). The geometric diameter is the equivalent volume diameter. Particles larger than  $10\ \mu\text{m}$  are deposited with nearly 100% efficiency. Below this size, the efficiency decreases to a minimum of approximately 20% at a size between  $0.3$  and  $1.0\ \mu\text{m}$ . The diffusion mechanism is responsible for the increased efficiency below  $0.3\ \mu\text{m}$ .

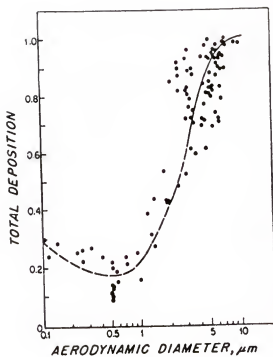


Figure 1-2. Total deposition in human respiratory tract. Source: Hinds, 1982, pg. 217.

### Characteristics of Test Aerosols

A log-normal distribution is often selected to describe a test aerosol. Three parameters are required to define this type of distribution: a median diameter, a concentration parameter, and the geometric standard deviation (GSD). The mass median aerodynamic diameter (MMAD) and mass concentration (M) are used when an aerosol is presented on a mass basis. The MMAD is the aerodynamic diameter for which half of the mass is contributed by particles larger than the MMAD and half by particles smaller than the MMAD. The GSD is a measure of the broadness in distribution of the aerosol. A monodisperse aerosol consists of particles of one size and has a GSD equal to 1.0. An aerosol with GSD ranging from 1.0 to 1.5 is considered to be narrowly distributed and a GSD above 2.0 indicates a highly polydisperse aerosol. If an aerosol follows a perfect log-normal distribution, the relationship between number median aerodynamic diameter (NMAD) and MMAD should follow the Hatch-Choate equation (Hinds, 1982):

$$\text{MMAD} = \text{NMAD} \exp(3 \ln^2(\text{GSD})) \quad (1-1)$$

An ideal inhalation test aerosol would be of sufficient mass concentration and would be monodisperse with particles of the precise size to be deposited in the desired target area. Unfortunately, monodisperse aerosol generators do not provide sufficient mass concentration to be practical in full-body exposure chambers. On the other hand,

the atomization process produces aerosols with sufficient mass concentration, but with highly polydisperse size distributions. In order to obtain an aerosol appropriate for use as a test aerosol, it is often necessary to segregate the desired narrow size range from a polydisperse aerosol.

#### EPA Human Exposure Laboratory

One of the major responsibilities of the Environmental Protection Agency (EPA) is to establish air quality standards which protect human health and welfare. To perform experimental research necessary to properly satisfy this role, EPA has built and operated a human exposure facility on the campus of the University of North Carolina at Chapel Hill for nearly twenty years. Currently, EPA is upgrading and relocating these facilities in a new building, in order to better provide experimental laboratories for research on humans.

The assessment of adverse health effects of atmospheric aerosol and gaseous pollutants on the human respiratory system is one of the health related topics of concern. The new building will house two room-size exposure chambers to evaluate the nature of exposure and severity of their effects. For the assessment of aerosol pollutants, the human exposure research will focus on water soluble aerosols. Table 1-1 lists the required ranges in aerosol size, mass concentration, and geometric standard deviation for the human exposure chamber.

Table 1-1. Aerosols needed in EPA human exposure chamber.

---

Aerosol Size	0.1 - 10 $\mu\text{m}$
Mass Concentration	0 - 2 $\text{mg}/\text{m}^3$
Geometric Standard Deviation	< 1.5
Maximum Mass Flow Rate	225 $\text{mg}/\text{min}^*$

---

\*Based on a maximum air flow rate of 112.5  $\text{m}^3/\text{min}$  @ 2  $\text{mg}/\text{m}^3$ .

### Project Objectives

The project goal was to develop a high-output, size-selective aerosol generator satisfying the need for test aerosols in EPA human exposure chambers. The aerosol generator was designed to produce a water-soluble aerosol with a mass median aerodynamic diameter varying from 1 to 10  $\mu\text{m}$  and a geometric standard deviation less than 1.5. Furthermore, the aerosol generator, upon replication, needs to supply a maximum aerosol mass flow rate of 225 mg/min for the human exposure chamber. In this project, generation of narrowly size-distributed solid particles involves three steps: producing liquid droplets, separating larger droplets from the aerosol airstream, and evaporating the size-selected liquid droplets to form solid particles.

Droplet generation is performed by a simplex or pressure-swirl atomizer, in which a swirling motion is imparted to the liquid so that it forms a conical aerosol sheet as soon as it leaves the orifice. Figure 1-3 shows a schematic diagram of the solid-cone simplex nozzle employed in the generator. It consists of a one-piece cast body with a removable vane-type core. This core features a cylindrical hole that serves as a plain-orifice atomizer to provide droplets at the center of the conical spray pattern. The solid-cone nozzle produces relatively coarse liquid droplets and the droplets at the center of the spray are larger than those near the periphery (Lefebvre, 1989).

Droplet separation is accomplished with an improved virtual impactor. In a conventional virtual impactor (Figure 1-4(a)), particle-laden air is accelerated through a nozzle impinging into a receiving tube that is slightly larger in diameter than the nozzle. The particles larger than the cut size of the virtual impactor have enough inertia to



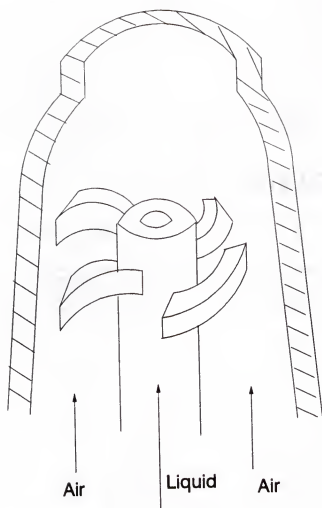


Figure 1-3. Schematic diagram of a solid-cone simplex nozzle.

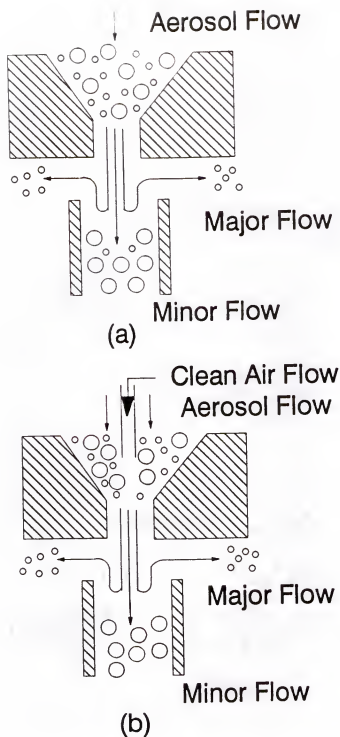


Figure 1-4. Schematic diagram of virtual impactors.

a) a conventional virtual impactor, b) an improved virtual impactor.

penetrate deep into the receiving tube and follow the minor flow ( $Q_a$ ) which is usually about 10% of the total flow ( $Q_t$ ). The major flow ( $Q_w$ ), containing particles smaller than the cut size, makes a sharp turn in the receiving tube and exits at the outer edges of the entrance to the tube. However, as a result of drawing a minor flow through the receiving tube, the coarse particle flow contains a small amount of fine particles. An improved virtual impactor (Figure 1-4(b)) employs a central clean air flow ( $Q_c$ ) to reduce (or eliminate) the fine particle contamination in the minor flow. The clean air core prevents small particles from entering the center of the acceleration nozzle and, therefore, small particles can follow the major flow air streamline and are separated more easily.

Evaporation is the last step to generate narrowly size-distributed solid particles. Larger droplets following the minor flow are subsequently diluted with clean, dry air and evaporated to form solid particles with narrow size distributions.

### Project Accomplishments

A high-output, size-selective aerosol generator capable of generating a narrow size-distribution aerosol with high mass concentrations was designed, fabricated, and tested at the University of Florida. Aerosols generated from a sodium chloride solution (0.05% to 9% by volume) were found to have a mass median aerodynamic diameter varying from 1.38 to 9.99  $\mu\text{m}$ , with a geometric standard deviation ranging from 1.18 to 1.46. Aerosol generation rate varied from 0.21 to 23.8 mg/min depending upon the particle size produced. To achieve a desired aerosol generation rate, 225 mg/min, for the EPA exposure chamber, the aerosol mass median aerodynamic diameter has a practical limit

to values between 3 and 9  $\mu\text{m}$ . This developed aerosol generator will be employed to produce water-soluble test aerosols for EPA's human exposure laboratory, located on the campus of the University of North Carolina at Chapel Hill.

## CHAPTER 2 REVIEW OF LITERATURE

### Background

Inertial impactors have been used extensively for nearly a half-century to collect airborne particles according to their aerodynamic sizes. In the solid-plate or real impactor, a flat plate is placed such that the surface is perpendicular to the air flow at the exit of a particle acceleration nozzle. Particles larger than the cut size of the impactor will slip across the air streamlines and impact upon the plate while smaller particles will follow the streamlines and not be collected. A well-designed impactor has a sharp collection efficiency curve. However, particle-surface interaction problems associated with the real impactor such as particle bounce, re-entrainment, break-up, and collection-surface overload have led to non-ideal performance and introduced inaccuracy into the data interpretation.

A virtual impactor, first developed almost simultaneously by Hounam and Sherwood (1965) and Conner (1966), is very similar to a real impactor, with the main difference being that the impaction plate has been replaced by a "virtual" surface (collection probe). Virtual impaction eliminates particle bounce and re-entrainment problems occurring in real impactors. In a virtual impactor, particle-laden air is accelerated through a nozzle impinging into the collection probe or receiving tube that

is slightly larger in diameter than the nozzle. The particles larger than the cut size of the virtual impactor have enough inertia to penetrate deep into the receiving tube and follow the minor flow. The minor flow rate is usually 5 to 10 percent of the total flow rate. The major flow containing particles smaller than the cut size, makes a sharp turn in the receiving tube and exits at the outer edges of the entrance to the tube. However, as a result of drawing a minor flow through the receiving tube, the coarse particle flow contains a small amount of fine particles. In a virtual impactor, particles both smaller and larger than the cut size of the virtual impactor remained airborne, and both can be either measured by a particle counter or collected by filtration.

### Conventional Virtual Impactors

A conventional virtual impactor is a one-stage, single-jet, laminar-flow impactor. The jet shape is either circular or rectangular and the total air volumetric flow rate is not high ( $< 50$  L/min) through the acceleration nozzle. Both theoretical and experimental studies have been performed by many investigators on round-jet or rectangular-slit-jet virtual impactors. The results of their studies are reviewed below.

### Round-Jet Virtual Impactors

Theoretical studies. Analytical studies on round-jet, laminar-flow virtual impactors have been conducted by Hasson et al. (1979) and more thoroughly by Marple and Chien (1980). Marple and Chien first determined the flow field within the impactor by solving the full Navier-Stokes equation using numerical analysis techniques, and then integrated

the particle equation of motion to solve for particle trajectory. The effects of the nozzle flow Reynolds number ( $Re$ ), the fraction of flow passing through the collection probe, and the physical dimensions of the nozzle throat and collection probe on particle separation and internal loss were investigated theoretically. Their results indicate that the shape of the large particle collection efficiency curves are not greatly influenced by any of these parameters. The only parameter that appears to affect the shape is minor flow ratio (minor flow rate divided by total flow rate). The reason for this is that the collection efficiency curves are asymptotic to the different values of minor flow ratio at low values of square root of Stokes number ( $Stk^{1/2}$ ). However, the internal losses are influenced by many of the parameters and, theoretically, have a maximum value as high as 70% occurring at the value of the particle diameter corresponding to 50% collection efficiency.

Experimental calibration. Calibrations of two round-jet, laminar-flow virtual impactors have been conducted by Chen et al. (1985). They used monodisperse solid polystyrene latex (PSL) and liquid dioctyl phthalate (DOP) aerosols to determine the collection efficiency curves. They have shown experimentally that the steepness of the collection efficiency curves are not very sensitive to value changes of  $Re$ , nozzle to probe distance ( $S$ ), and receiving tube diameter ( $D$ ) and that the 50% cut-off Stokes number ( $Stk_{50}$ ) is substantially affected by the minor flow ratio as the theory predicts (Marple and Chien, 1980). In addition, they suggest that the separation efficiency curve is not identical for solid and liquid aerosols because of the existence of internal circulation in liquid droplets at the acceleration nozzle.

Particle loss. One of the major concerns of virtual impactor design is to minimize particle loss. Loo and Cork (1988) developed a high efficiency virtual impactor which has a cutpoint diameter of 2.5  $\mu\text{m}$  and wall loss of under 1%. They have demonstrated that a virtual impactor with very low internal wall losses is attainable despite theoretical predictions to the contrary. According to their explanation, this discrepancy is probably due to the inadequately fine definition of details for computations conducted at the critical regions of particle separation in the analysis of Marple and Chien (1980).

#### Rectangular-Slit Jet

Both theoretical and experimental work have been done on the two-dimensional slit virtual impactor (Ravenhall et al., 1978, 1982; Forney et al., 1982). One advantage of a rectangular slit virtual impactor is that the collection efficiency can be easily determined over a range of Stokes number (Stk) with the same test aerosol of fixed particle diameter by simply adjusting the slit widths. The virtual impactor used by Forney et al. (1982) has a variable slit width which allows one to easily calibrate the instrument. Their experimental results show that the internal particle loss has a minimum value of seven percent as the normalized void width increases to 1.6. Theoretically, internal particle losses should reduce to zero as the normalized void width increases to 1.4 (Ravenhall et al., 1982). Increasing the void width, however, is shown to substantially reduce the steepness of the particle collection efficiency curves for both theoretical and experimental data.



### Multi-Stage and Parallel-Stage Virtual Impactors

Virtual impactors may be arranged in multi-stage or parallel-stage units. Loo et al. (1976) developed a two-stage virtual impactor for large scale monitoring of airborne particulate matter, with three parallel jets for the inlet stage and a single jet for the second stage. McFarland et al. (1977) designed a multiple-jet virtual impactor with 25 jets in parallel to collect kilogram quantities of size-fractionated particulate matter which can be subsequently used for biologic testing purposes. In this device, a total flow rate as high as 850 L/min is achieved and the particle cut size is reported to be 5.2  $\mu\text{m}$ . Novick and Alvarez (1987) designed a two-stage virtual impactor to measure particle size distributions by determining the MMAD and GSD. Marple et al. (1990) developed a High-Volume Virtual Impactor (HVVI) to fractionate the PM-10 (total particulate matter less than 10  $\mu\text{m}$ ) mass into a fine (0-2.5  $\mu\text{m}$ ) and coarse (2.5-10  $\mu\text{m}$ ) aerodynamic diameter range. The HVVI assembly defined as a parallel stage virtual impactor contains 12 identical virtual impactor stages in a parallel flow arrangement.

### Virtual Impactors with Central Clean Air Cores

Particle separation characteristics of conventional virtual impactors may be improved by introducing a clean air core in the center of the acceleration nozzle. This clean air flow is used to reduce (or eliminate) the contamination of small particles in the minor flow. Masuda et al. (1979) developed an improved virtual impactor that reduced contamination by confining the aerosol flow between a core of clean air and an enveloping sheath of clean air. They suggest that an increase in the ratio of clean air

flow rate to aerosol flow rate improves the particle separation quality. Unfortunately, the separation falls below the predicted value if there is a distortion of the annular aerosol flow. Chen et al. (1986) designed and evaluated an improved virtual impactor with a clean air core in the center of the acceleration nozzle. Their results show that a stable, precise separation of aerosol particles is attainable with the use of a clean air core. Chen and Yeh (1987) reported that their virtual impactor with a clean air core has small wall losses (<5%) and little or no fine particle contamination. They have identified and presented important design parameters which affect wall losses and separation characteristics of an improved virtual impactor.

#### Turbulent-Flow and Counterflow Virtual Impactors

Turbulent-flow. A single-jet, high-volume virtual impactor was developed by Solomon et al. (1983). This device is operated at 500 L/min and has an aerodynamic particle cutpoint diameter of about 2 to 3  $\mu\text{m}$ . Under these conditions, the flow through the acceleration nozzle is calculated to be turbulent. Their experimental studies indicate that this virtual impactor can separate particles according to aerodynamic diameter as efficiently as the laminar-flow virtual impactor. The data show that over the range of Reynolds numbers from 24,000 to 81,000 there is little, if any, dependence of inferred acceleration nozzle turbulence on the performance characteristics of the sampling system. Their analyses also indicate that the performance characteristics of this turbulent-flow virtual impactor can be described by the same theory that describes both real and virtual laminar flow impactors.

Counterflow. Fine particle contamination in the minor flow of a conventional virtual impactor may be reduced by introducing a clean air flow opposite to the direction of the aerosol flow in the collection probe. Ogren et al. (1985) employed the concept of counterflow in the design of virtual impactor and developed the initial version of counterflow virtual impactor for aircraft fog sampling. Noone et al. (1988) calibrated a counterflow virtual impactor. Their experimental results showed that the impactor behaves in accordance with theoretical predictions using Stokes number calculation. Anderson et al. (1993) presented a new method to calibrate a counterflow virtual impactor at aerodynamic diameters from 1 to 15  $\mu\text{m}$ . The results indicate that this impactor has a sharp collection efficiency curve and is well suited for studying aerosol effects on cloud microphysics.

### Applications

Particle counters. Virtual impactors can be used to mitigate the problems of small particle coincidence and insufficient concentrations of large, high-inertia particles for particle counters. Barr et al. (1983) designed an aerosol concentrator using the virtual impaction principle to increase the number concentration of an aerosol above the design cutpoint size. Keskinen et al. (1987) introduced the idea of a virtual impactor to increase the sensitivity of Optical Particle Counters (OPCs) for large particles and suggested the possible applications of filter testing and cleanroom measurements. Shortly thereafter, Wu et al. (1989) used a virtual impactor as an aerosol concentrator to increase the particle concentration for cleanroom monitoring. Liebhaber et al. (1991) developed a low-cost

virtual impactor with a 37-mm cassette, hypodermic needles, and common laboratory items for large-particle amplification in OPCs. These techniques have been shown to have a significant amplification of the large-particle concentration and therefore, reduce small-particle coincidence errors and large-particle statistical errors in OPC measurements.

Generation of aerosols of narrow size range. Virtual impactors can be employed to produce an aerosol with a narrow size distribution. Masuda et al. (1978) successfully employed a set of two virtual impactors to prepare test aerosols with narrow size distributions from actual coal dust and slate powder. Chen et al. (1988) confirmed that two round-jet, in-series virtual impactors have the potential to be used as a quasi-monodisperse aerosol generator. Their experimental results showed that powder aerosols with GSD values less than 1.22 can be obtained by passing fly ash and oil shale aerosols through this device. Pilacinski et al. (1990) used a virtual impactor to modify the size distribution of aerosols generated from a modified Wright nebulizer. Recently, Chein and Lundgren (1993) developed a virtual impactor with clean air core to generate test aerosols with narrow size distributions. This impactor employs four sets of interchangeable nozzles and probes. The cut size of the virtual impactor can be varied from 1 to 10  $\mu\text{m}$ . An aerosol with a MMAD varying from 0.98 to 10  $\mu\text{m}$  and a GSD ranging from 1.16 to 1.48 is successfully generated with this impactor.

## CHAPTER 3 MATERIALS AND METHODS

### Description of the Aerosol Generator

A schematic diagram of the high-output, size-selective aerosol generator (HOSSAG) is shown in Figure 3-1. The HOSSAG consists of two sections: aerosol generation and segregation. Droplet generation is performed by a Delavan solid-cone simplex nozzle #30610-4 (stainless steel) which has exactly identical geometric dimensions as the testing nozzle #30609-5 (brass). It was installed in a polyvinyl chloride (PVC) chamber, 15 cm (6 inch) in diameter and 152 cm (60 inch) in length. Figure 3-2 shows an assembly view of the PVC generation chamber. The nozzle plate could be easily removed from the generation chamber if the spray nozzle needs to be cleaned. To clean the spray nozzle, the spray nozzle could be operated at normal atomization pressure for about five minutes with the nebulizing air line filled with about 200 cm<sup>3</sup> of clean water and the liquid line directed into a clean water reservoir.

Droplets generated by the simplex nozzle passed through an improved virtual impactor which segregated particles according to their aerodynamic diameters. The particle segregation section was made out of aluminum except the clean air tube which was stainless steel. The aluminum material was anodized to prevent corrosion caused by reactive aerosols. A liquid drain was employed to drain off excess liquid if

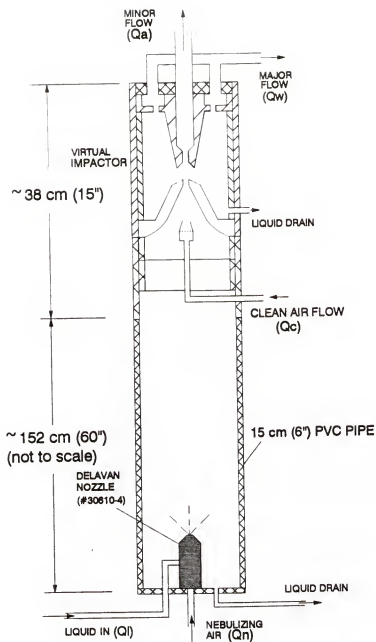


Figure 3-1. Schematic diagram of the high-output, size-selective aerosol generator.

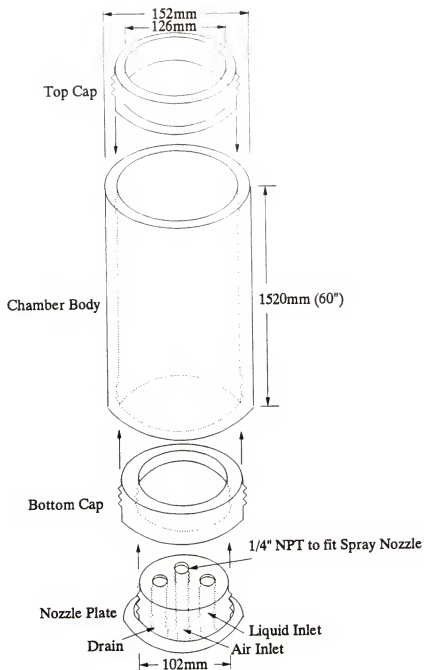


Figure 3-2. An assembly view of the aerosol generation chamber.

liquid droplets accumulated inside the virtual impactor after a long period of operation. The total height and diameter of the HOSSAG were about 190 cm (75 inch) and 15 cm (6 inch), respectively.

### Improved Virtual Impactors

#### Theoretical Equations

According to Chen et al. (1986), the separation efficiency,  $\eta$ , of a monodisperse aerosol sampled with the collection probe of an improved virtual impactor is given by the following two equations:

$$\eta = 0 \quad \text{for } 0 \leq r_c < r_1 \quad (3-1)$$

$$\eta = (\eta_0 - \omega) / (1 - \omega) \quad \text{for } r_1 \leq r_c \leq r_2 \quad (3-2)$$

where

$\eta_0$  = separation efficiency of a conventional virtual impactor

$\omega$  = clean air flow ratio (=  $Q_c / Q_t$ )

$r_1$  = radius of the central clean air flow

$r_2$  = nozzle radius (=  $W/2$ )

$r_c$  = critical radius within which the accelerated particles are separated from the major flow and pass into the minor flow (shown in Figure 3-3).



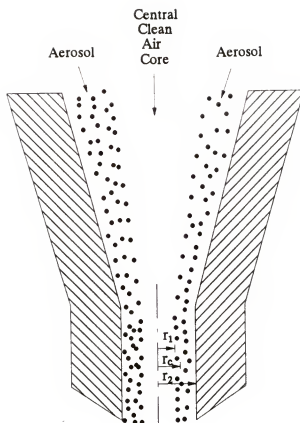


Figure 3-3. Schematic diagram of the aerosol flow with the central air core in the acceleration nozzle.

The equations indicate that the separation efficiency ( $0 \leq \eta \leq 1$ ) of the improved virtual impactor can be computed by knowing the values of  $\eta_0$  and  $\omega$ . For given values of  $\eta_0$  and  $\omega$ ,

$$\eta = \begin{cases} 1, & \eta_0 = 1 \\ (\eta_0 - \omega) / (1 - \omega), & \omega < \eta < 1 \\ 0, & 0 \leq \eta_0 \leq \omega \end{cases} \quad (3-3)$$

Based on Equation 3-3, fine particle contamination in the minor flow decreases for the improved virtual impactor because the efficiency  $\eta$  is equal to 0 when  $\eta_0$  is less than or equal to  $\omega$ . The separation efficiency curve of the improved virtual impactor has a steeper slope (better cutoff characteristics) than the conventional virtual impactor due to the fact that  $\eta$  is smaller than  $\eta_0$  when  $\eta_0$  is less than 1.

The cutoff characteristic of an improved virtual impactor can be described by the dimensionless Stokes number,  $Stk$ , which is defined for an impactor as the ratio of particle stopping distance at the average nozzle exit velocity  $V_0$  to the nozzle (jet) radius,  $W/2$  (Hinds, 1982, p. 114).

$$Stk = \tau V_0 / (W/2) = \rho_p C d^2 V_0 / 9 \mu W \quad (3-4)$$

where

$\tau$  = particle relaxation time

$\rho_p$  = particle density

$C$  = Cunningham correction factor for a particle of diameter  $d$

$V_0$  = average fluid velocity at the nozzle exit

$\mu$  = fluid viscosity.

The Cunningham correction factor is used to account for particle slip effects in the Stokes's law as particle sizes approach the mean free path of the gas and is given by the following equation:

$$C = 1 + \lambda/d ( 2.514 + 0.800\exp(-0.55d/\lambda) ) \quad (3-5)$$

where

$\lambda$  = gas mean free path

For the mechanical behavior of two particle-fluid systems to be similar in an impactor, it is essential to have geometric, hydrodynamic, and particle trajectory similarity. Hydrodynamic similarity is accomplished by fixing the Reynolds number for the flow in the impactor. Similarity of particle trajectories depends on the Stokes number based upon the equation of particle motion. Trajectory similarity also requires that the particle interception parameter ( $= d / (W/2)$ ) be preserved when particles come within one radius of the impaction surface at the same relative location. For Stokesian particles, two impaction regimes are similar when the Stokes, Interception, and Reynolds numbers are the same (Friedlander, 1977, p. 98).

Experimental studies of improved virtual impactors (Chen and Yeh, 1987) indicate that, as long as the minor flow ratio,  $\gamma$  ( $=Q_a/Q_t$ ), is approximately 9%, the clean air flow ratio,  $\omega$ , is equal to or greater than  $2\gamma$  and the Reynolds number is between 1000 and 8000, the dimensionless parameter  $(Stk)^{1/2}_{50}$  [value of the  $(Stk)^{1/2}$  for which the separation efficiency is 50%] is 0.86 for both solid polystyrene latex and liquid dioctyl phthalate aerosols with the maximum wall loss ( $< 5\%$ ) occurring near this cutoff value. Knowing this, the cutoff aerodynamic diameter,  $d_{50}$ , can be estimated for other geometrically and dynamically similar virtual impactors with a nozzle diameter  $W$ :

$$d_{50}(\mu m) = [ 5.7 W^3(mm) / C Q_t(lpm) ]^{1/2} \quad (3-6)$$

### Design Approaches

An improved virtual impactor with a very sharp separation efficiency curve (little or no fine particle contamination) and little wall loss is very important for the HOSSAG to successfully generate test aerosols with narrow size distributions and high mass concentrations. The impactor should be able to operate for an extensive period without reduction in separation efficiency and any nozzle clogging problems. In addition, this impactor should have a wide range of selectable cut sizes so that the HOSSAG is able to generate test aerosols with MMAD varying from 1 to 10  $\mu m$ .

Based upon the above design criteria, an improved virtual impactor was designed, fabricated, and employed in the HOSSAG. Figure 3-4 shows a schematic diagram of the

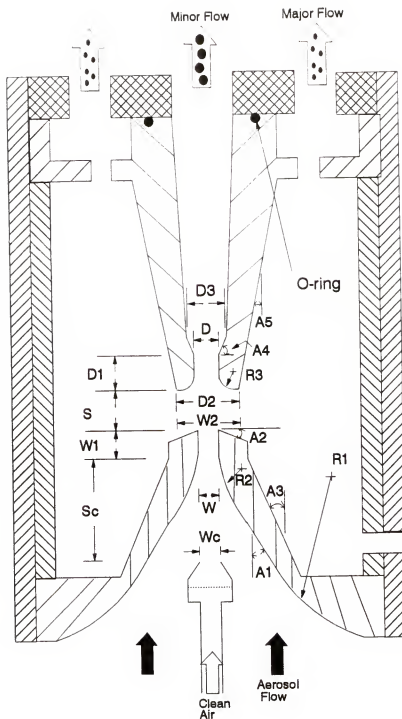


Figure 3-4. Schematic diagram of the improved virtual impactor.

improved virtual impactor indicating the important design parameters. Among those design parameters listed on the diagram, W, D, S, R3, Sc, and Wc are the most critical design parameters for the improved virtual impactor. Basic design features of the improved virtual impactor follow the work of Chein and Lundgren (1993). However, in the early testing phase of the virtual impactor, droplets were found to accumulate on the nozzle. In a short period of operation, they would gradually form a large droplet, partially blocking the nozzle. Droplet accumulation could change the nozzle diameter and make the performance of the virtual impactor unpredictable. Therefore, two important modifications on the nozzle design have been employed to avoid droplet accumulation on both the inlet and outlet of the acceleration nozzle. The first modification was a smooth transition region (a curve radius of R2 shown in Figure 3-4) at the inlet of the nozzle. The second modification was a 15° slope (A2) right after the nozzle outlet so that liquid can drain down.

Two sets of acceleration nozzles and collection probes for the virtual impactor were fabricated. They share the same housing and clean air section. A schematic diagram of the clean air section is shown in Figure 3-5. Table 3-1 shows the geometric dimensions of these two sets of virtual impactors with the same value of Wc (22.0 mm), A1 (30°), A2 (15°), A3 (30°), A4 (45°), and A5 (15°). Figure 3-6 shows a photograph of the virtual impactor with the clean air tube employed in the HOSSAG. Detailed design drawings of the aerosol generation chamber, the improved virtual impactor, and the clean air section are compiled in the Appendix.

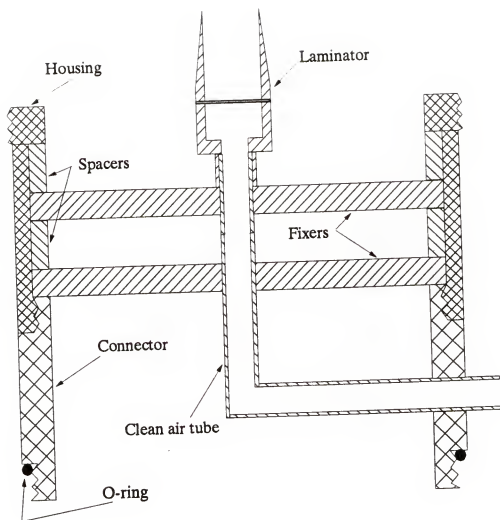


Figure 3-5. Schematic diagram of the clean air section.

Table 3-1. Geometric dimensions of the improved virtual impactor set I and II  
( $W_c=22.0$  mm,  $A1=30^\circ$ ,  $A2=15^\circ$ ,  $A3=30^\circ$ ,  $A4=45^\circ$ , and  $A5=15^\circ$ ).

Set #	W (mm)	W1 (mm)	W2 (mm)	D (mm)	D1 (mm)	D2 (mm)	D3 (mm)	S (mm)	Sc (mm)	R1 (mm)	R2 (mm)	R3 (mm)
I	10.0	10.0	30.0	15.0	10.0	30.0	24.0	10.0	45.0	42.0	2.4	3.0
II	15.0	15.0	45.0	22.5	15.0	45.0	28.5	15.0	35.0	49.4	3.6	4.5





Figure 3-6. Photograph of the virtual impactor with the clean air tube.

The average air velocity and Reynolds number at the entrance of the improved virtual impactor (exit of the gravity separation section) was calculated to be 6.5 cm/sec and 450, respectively, at the nebulizing air flow rate of 47 lpm. As the air was accelerated to the nozzle exit, at a total flow rate of 62 lpm for virtual impactor set I, the average air velocity and Reynolds number were dramatically increased to 1320 cm/sec and 8800, respectively. For virtual impactor set II, the average air velocity and Reynolds number were 700 cm/sec and 7000, respectively, at a total air flow rate of 74 lpm.

Clean air flow rate was set to 15 lpm for virtual impactor set I. The average air velocity in the clean air tube was calculated to be 66 cm/sec. Average air velocity in the clean air tube was 118 cm/sec at an air flow rate of 27 lpm for virtual impactor set II. It was expected that the average clean air flow velocity needed to be slightly larger than the average aerosol flow velocity in the improved virtual impactor to prevent small particles from entering the clean air core and, therefore, improve the particle separation efficiency. However, high velocity differences induce vortex between two different velocity field, so the velocity difference between the clean air flow and aerosol flow should be kept to minimum. Calculations could be made to estimate the appropriate  $Sc$  value for the clean air flow to work efficiently. For example, at  $Q_n = 47$  lpm,  $Q_c = 15$  lpm, and  $Sc = 40$  mm, the average clean air flow velocity and aerosol flow velocity was calculated to be 66 and 38 cm/sec, respectively, in virtual impactor I. At  $Q_n = 47$  lpm,  $Q_c = 27$  lpm, and  $Sc = 20$  mm, the average clean air flow velocity and aerosol flow velocity was calculated to be 118 and 104 cm/sec, respectively, in virtual impactor II.

## Aerodynamic Particle Sizer

### Operating Principle

The Aerodynamic Particle Sizer (APS, model 3310, TSI, Inc., St. Paul, MN) was used to measure particle size distributions of test aerosols generated by the HOSSAG. Figure 3-7 shows a schematic diagram of the Aerodynamic Particle Sizer. In the APS, particles are introduced into the center of an accelerating nozzle. Small particles follow the motion of the air closely while larger particles lag behind due to their greater inertia. Particle velocities are determined by measuring the time of flight taken by individual particles to travel between two laser beams. The laser beams are separated by a constant distance (~120  $\mu\text{m}$ ) and located near the exit of the accelerating nozzle. Particle transit time between the two laser beams depends mainly upon their aerodynamic diameter. Larger particles are accelerated to lower final velocities due to their greater inertia and, therefore, have longer transit times than smaller particles. The air velocity at the exit of the outer nozzle in the APS can be estimated by the Bernoulli equation for compressible, ideal gases (Chen et al., 1985):

$$V_g = \left[ (2RT/M.W.) \ln(P/(P-\Delta P)) \right]^{1/2} \quad (3-7)$$

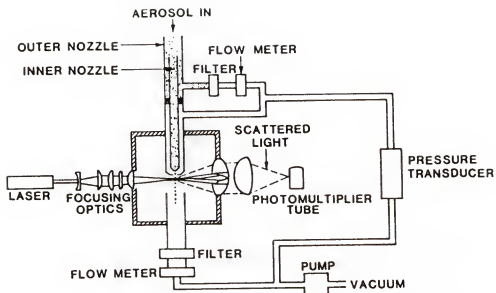


Figure 3-7. Schematic diagram of the aerodynamic particle sizer.  
Source: Cheng et al., 1993.

$V_g$  = the centerline air velocity (m/sec)

$P$  = upstream (ambient) pressure

$\Delta P$  = pressure drop between the sampling inlet and the  
detection tube.

$T$  = temperature ( $^{\circ}\text{K}$ )

$R$  = gas constant (8.31 J/K-mole)

M.W. = molecular weight of the air (0.0289 Kg/mole).

The APS measures particle sizes by determining their velocities relative to the air velocity ( $\sim 150$  m/sec). This velocity is compared with a calibration curve which is established using monodisperse spheres.

### Calibration

Spherical particles of polystyrene latex (PSL, density of  $1.05 \text{ g/cm}^3$ ) and polyvinyl toluene (PVT, density of  $1.21 \text{ g/cm}^3$ ) are used to calibrate the APS at the factory under ambient conditions (740 mmHg and  $20^{\circ}\text{C}$ ). The calibration of each APS instrument is unique due to variations in the nozzle sizes, spacing, and laser beam locations. If the APS is used at operating conditions different from the calibration condition, then it should be recalibrated using monodisperse spheres. However, a single-velocity method developed by Rader et al. (1990) could be alternately employed to adjust the operating conditions so that the factory calibration curve can be used with minimum error. This method is based on the observation that if the gas velocity of the APS is maintained at

a single value, then a particle will also move at the same velocity regardless of operating conditions (Chen et al., 1985 and Rader et al., 1990). The procedure for determining the appropriate operating condition for the single-velocity method is as follows:

1. Calculate  $V_g$  using Equation 3-7 for  $P=740$  mmHg,  $T=293$  K, and  $\Delta P$  from the factory data sheet. This value should be close to 150 m/sec.
2. Calculate  $\Delta P$  using Equation 3-7 and the  $V_g$  obtained from the previous step for local temperature and pressure.
3. Adjust the total flow of the APS so that the pressure drop is equal to the value obtained in the step 2.
4. Set the ratio of the sheath air flow to the aerosol flow equal to 4.

Due to the difference in ambient conditions between TSI and the University of Florida laboratory, the single-velocity method is employed in this project to determine particle size distributions.

#### Non-Stokesian Corrections

The APS accelerates an aerosol and produces particle Reynolds number outside the Stokes regime where particle aerodynamic diameters are traditionally defined. Particle Reynolds numbers in the APS sensing volume are estimated to be from 1.16 to 163 for 1 to 20  $\mu\text{m}$  particles (Baron, 1986). Therefore, the measured size is dependent on other factors such as gas density, viscosity, particle density, and particle shape in addition to

the aerodynamic diameter. The acceleration of an aerosol can be determined according to the following equation if we neglect the Cunningham correction which is close to unity for particles larger than 2  $\mu\text{m}$  (Marshall et al., 1991):

$$dU/dt = 3\mu U/(d_{ae})^2 \left[ 6/\rho_0 + (\rho_a U d_{ae}/\rho_0 \mu)^{2/3} \cdot (\chi/\rho_p) \right] \quad (3-8)$$

where

$U$  = particle velocity relative to air velocity

$t$  = time interval associated with particle acceleration

$\mu$  = air dynamic viscosity

$d_{ae}$  = particle aerodynamic diameter

$\rho_0$  = reference particle density of 1000  $\text{kg/m}^3$

$\rho_a$  = air density

$\chi$  = particle dynamic shape factor

Spherical particles of higher density appear as larger particles in the APS because of the smaller drag force (smaller acceleration) experienced by a dense sphere with the same aerodynamic diameter (Chen et al., 1990). On the other hand, nonspherical particles with a dynamic shape factor greater than one appear as smaller particles (than spherical particles of the same aerodynamic diameter) because of the larger drag force (larger acceleration) experienced by the nonspherical particles (Cheng et al., 1990).

Corrections can be derived for the APS response to particles of arbitrary density and shape by equating their acceleration with the acceleration of particles of known density and shape used to calibrate the instrument (Wang and John, 1987). Marshall et al. (1991) give the following equation for the correction:

$$d_{se} = d_{APS} \left\{ \frac{[6+(R_{se})^{2/3}]^{1/2}}{[6+(R_{APS})^{2/3}]^{1/2}} \right\} \quad (3-9)$$

where

$$R_{se} = U\rho_a/\mu (\rho_0\chi/\rho_p)^{1/2} d_{se}$$

$$R_{APS} = U\rho_a/\mu (\rho_0\chi_e/\rho_e) d_{APS}$$

$d_{APS}$  = particle aerodynamic diameter measured by APS

$\chi_e$  = dynamic shape factor of calibrant particles

$\rho_e$  = calibrant particle density

While the density correction reported by Wang and John (1987) has been incorporated in the APS software, the particle shape correction has never been accounted for. Marshall et al. (1991) reported that regular-shaped solid particles ( $\chi=1.19$ ) in the size range from about 6 to 14  $\mu\text{m}$  aerodynamic diameter are underestimated by an average of 25% when using the APS.

Solid sodium chloride particles ( $\rho_p=2.2 \text{ g/cm}^3$ ,  $\chi=1.08$ ) were generated and measured by the APS in the course of this research. The density correction was performed by the APS software automatically, but the shape correction was not executed due to the lack of an automatic correction program. In addition, the effect on the overall



size distributions of sodium chloride particles was not considered to be significant due to the relatively small value of  $\chi$ .

### Coincidence Effects

Like all single particle analyzing instruments, the APS produces coincidence errors if a second particle enters the measuring volume while the first one is still present. The coincidence error level is concentration-dependent and produces randomly size-distributed false counts. If a high concentration of particles is present at the lower size detection limit of the instrument, there is a high probability that a particle is only detected when it either enters or leaves the sensing volume. This causes the recording of randomly sized phantom particle counts. The phantom particle and coincidence error problems of time of flight spectrometry like the APS are described in detail by Heitbrink et al., 1991.

An automatic reduction program of both phantom and coincidence counts has been developed (Horn, 1993). This program was employed in this project to correct particle size distributions when the original APS data appeared to have severe coincidence and phantom counts. The program was also used to determine the MMAD, NMAD, and GSD by fitting a log-normal distribution curve on the APS data.

### Experimental Procedure

#### Testing of Spray Nozzles

In the beginning of this research, three Delavan simplex nozzles (#30610-1, #30609-2, and #30609-5) were tested over wide range of atomization pressures ( $P_A$ ) and

liquid pressures ( $P_L$ ) using 9% (by volume) sodium chloride solutions. The testing was intended to find a suitable spray nozzle which could produce a sufficient mass generation rate and proper droplet size distributions for later segregation to be performed by the improved virtual impactor.

Figure 3-8 shows the experimental set-up used to investigate the performance of the Delavan simplex nozzles. Three test conditions were arranged. The first test condition was performed with the spray nozzle #30609-2 in a 10-inch diameter PVC chamber and the dilution air 1 was used to make up the air flow necessary to move desired droplets. The second test condition employed the spray nozzles #30610-1 and #30609-2 in a 6-inch diameter PVC chamber and the dilution air 1 was not used. The last test condition employed the spray nozzle #30609-5 in the same 6-inch diameter PVC chamber without the dilution air 1.

The nebulizing air flow rate was measured with a calibrated wet test meter and the liquid flow rate was determined by measuring the volume of pure water atomized in a certain time interval. During the testing of spray nozzles, the improved virtual impactor was installed but not operating (major flow was plugged). The generated droplets were subsequently diluted and evaporated with the dilution air 2. Drawn by an ejector, a small portion of aerosol flow (~1.8 L/min) entered the isokinetic sampling probe. The aerosol concentration was further diluted with a TSI diluter to an acceptable level. Particle size distributions were measured by the APS and the mass generation rate (Ma) was determined by total filtration.

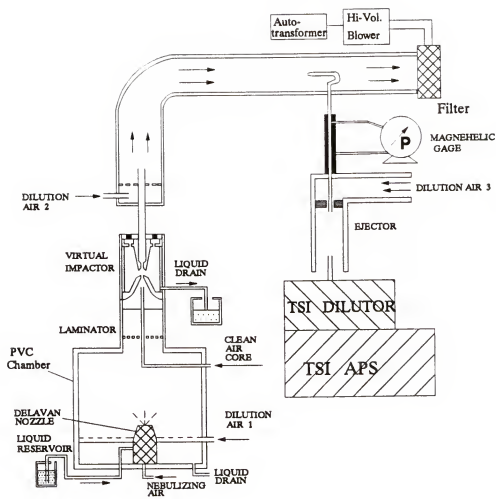


Figure 3-8. Experimental set-up used to test the Delavan simple nozzles.

### Evaluation of the HOSSAG performance

Figure 3-9 shows the experimental set-up used to evaluate the performance of the high-output, size-selective aerosol generator. A Delavan spray nozzle was selected to generate a cloud of salt water droplets from a sodium chloride solution, supplied by a liquid reservoir (open to ambient pressure) located at about 40 cm below the nozzle. The concentration of sodium chloride solution was varied from 0.05% to 9% (by volume) to change the MMADs of solid particles after the droplets evaporated. The spray nozzle was operated at the selected operating conditions ( $P_A=207$  kPa and  $P_L=-3.9$  kPa) based on the results of the nozzle testing. Nebulizing air flow rate ( $Q_n$ ) and liquid flow rate ( $Q_l$ ) were about 47 lpm and 2.15 lph, respectively.

Droplets generated by the simplex nozzle were subsequently segregated by the improved virtual impactor according to their aerodynamic diameter. Two sets of acceleration nozzles and receiving probes were used interchangeably to generate test aerosols of different MMADs. The major flow,  $Q_w$ , containing droplets less than the cut size passed through a glass fiber filter and a calibrated orifice meter. The minor flow,  $Q_a$ , carried off target droplets and mixed with dry, clean dilution air (~70 lpm) in a 4-inch diameter PVC pipe. Most of the droplets should evaporate and become smaller solid particles before entering the isokinetic sampling probe. A small amount of the aerosol flow (~1.8 lpm) was drawn by an ejector which diluted the aerosol concentration to an acceptable level for the APS measurement (minimum coincidence errors). The remaining flow went to another glass fiber filter which was used to determine the aerosol generation

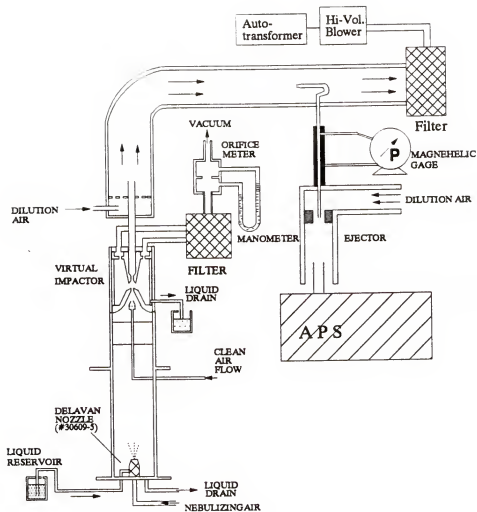


Figure 3-9. Experimental set-up used to evaluate the performance of the high-output, size-selective aerosol generator.

rate. Figure 3-10 shows the photograph of the evaluation system indicating the prototype aerosol generator.

#### Determination of Aerosol Size Distribution and Generation Rate

A glass fiber filter was used to collect the remaining aerosol as the APS was measuring the particle size distribution. Sampling time varied from about 7 to 40 minutes depending upon the aerosol concentration. During this period, the APS sampled at least three times to measure the particle size distribution. These three sets of data were grouped into one single size distribution. The filter was desiccated for 24 hours before and after use. Aerosol concentration was determined by desiccating and weighing the filter. A Sartorius balance with a sensitivity of 0.01 mg was used. A filter weight gain of about 10 mg was obtained for each sample. The filter weight gain was divided by the total sample time and it was slightly adjusted for the flow drawn by the ejector to give the true aerosol generation rate.

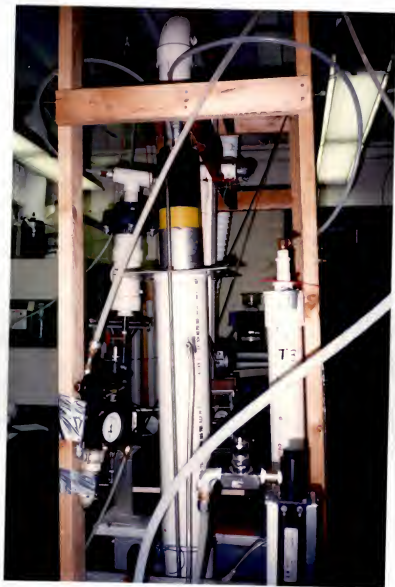


Figure 3-10. Photograph of the evaluation system showing the prototype aerosol generator.

## CHAPTER 4 RESULTS AND DISCUSSION

### Testing of Delavan Simplex Nozzles

#### Nozzle #30609-2

In the early testing stage of spray nozzles, the Delavan simplex nozzle #30609-2 was first selected and tested based on the recommendation of Gotsch (1994). The spray nozzle was installed on the bottom of the 10-inch diameter generation chamber. A sodium chloride solution of 9% (by volume) was used and the liquid pressure head was fixed at 0 cm of water (relative to the ambient pressure). The total air flow carrying the droplets upward was maintained at a constant value of 75 lpm for different atomization pressures by adjusting the flow rate of the dilution air 1. At this air flow rate, droplets larger than about 30  $\mu\text{m}$  were removed by gravitational settling in the generation chamber. In our aerosol laboratory experiments, the ambient pressure and temperature were typically  $760 \pm 10$  mmHg and  $24 \pm 1$  °C, respectively, so air flow rates mentioned in this project were measured based on these conditions.

Figure 4-1 shows the liquid flow rate and nebulizing air flow rate as a function of atomization pressure,  $P_A$ . The liquid flow rate reached its maximum value as the atomization pressure was increased to approximately 140 kPa (gage pressure). The



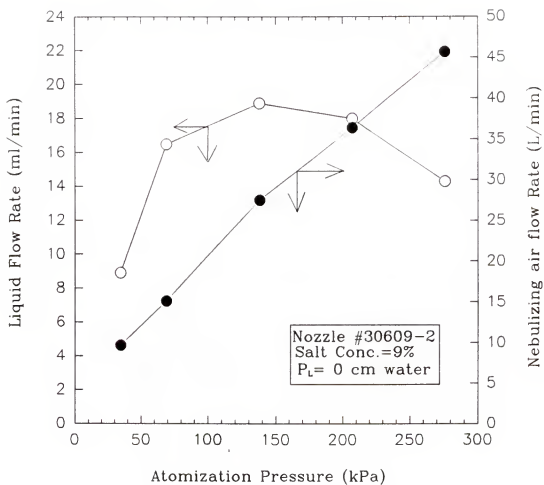


Figure 4-1. Liquid flow rate and nebulizing air flow rate as a function of atomization pressure for the Delavan simplex nozzle #30609-2.

nebulizing air flow rate increased as the  $P_A$  increased, which was expected. Figure 4-2 shows the aerosol generation rate,  $M_a$ , as a function of atomization pressure. The aerosol generation rate increased as the atomization pressure was increased and achieved its highest value ( $\sim 115$  mg/min) as the  $P_A$  was equal to around 210 kPa. Further increase of  $P_A$  caused the aerosol generation rate to decrease mainly due to the impaction loss on the wall of the generation chamber.

Figure 4-3 and 4-4 display the particle mass concentration histograms generated by the spray nozzle at different  $P_A$  values. The dotted line was the log-normal fitted curve used to determine MMAD and GSD values from the original APS data. At  $P_A = 69$  kPa, the MMAD and GSD were  $2.18\text{ }\mu\text{m}$  and 1.80, respectively. There was a significant amount of submicron particles which was not measured by the APS due to the lower detection limit ( $\sim 0.8\text{ }\mu\text{m}$ ) of the instrument. Therefore, the automatic reduction program was employed to reduce both phantom counts and coincidence errors. As the  $P_A$  value increased to 276 kPa, the MMAD was decreased to  $1.62\text{ }\mu\text{m}$  due to the fact that more small particles were produced at higher  $P_A$ . The GSD did not change significantly as the  $P_A$  was varied.

#### Nozzles #30609-2 and #30610-1

The spray nozzles #30609-2 and #30610-1 have identical geometric dimensions except that #30609-2 is made out of brass and #30610-1 is made out of stainless steel. These two nozzles were installed on the bottom of the 6-inch diameter PVC generation chamber and operated at  $P_A = 104$  kPa to achieve a total air flow rate of 55 lpm without

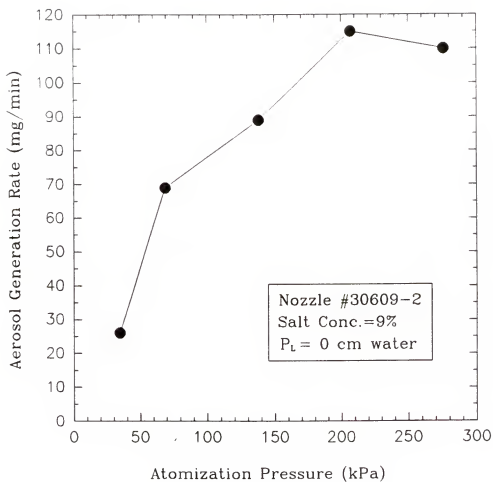


Figure 4-2. Aerosol generation rate as a function of atomization pressure for the Delavan simplex nozzle #30609-2.

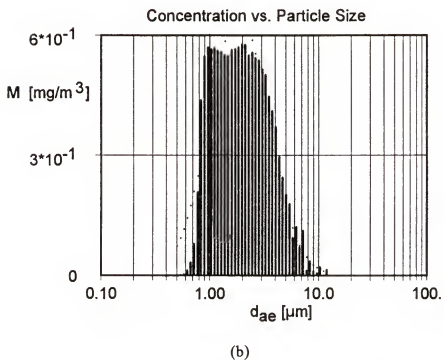
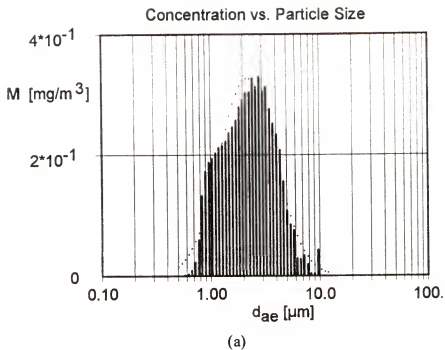
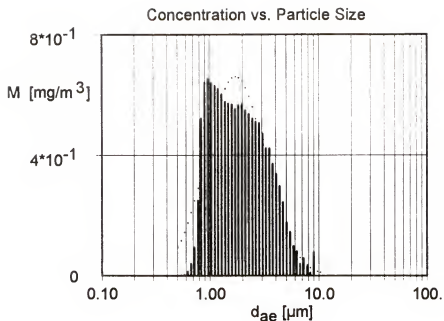
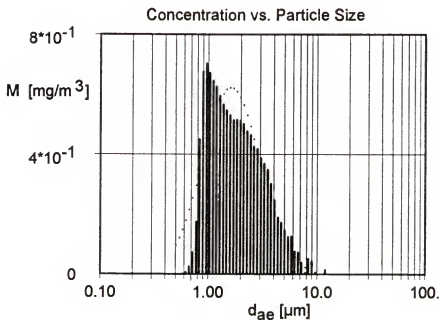


Figure 4-3. Particle mass concentration histograms generated by the simplex nozzle #30609-2 at different atomization pressures,  $P_A$ . The dotted point shows the log-normal fitting curve.

a)  $P_A = 69$  kPa; b)  $P_A = 138$  kPa.



(a)



(b)

Figure 4-4. Particle mass concentration histograms generated by the simplex nozzle #30609-2 at different atomization pressures,  $P_A$ . The dotted point shows the log-normal fitting curve.

a)  $P_A = 207 \text{ kPa}$ ; b)  $P_A = 276 \text{ kPa}$ .

using the dilution air 1. At this air flow rate, droplets larger than about 40  $\mu\text{m}$  were removed by gravitational settling in the generation chamber.

Figure 4-5 shows the aerosol generation rate as a function of liquid pressure,  $P_L$ . The aerosol generation rate reached its maximum value (~95 mg/min) as the  $P_L$  was equal to about 0 cm of water. Further increase of  $P_L$  caused the aerosol generation rate to decrease, which suggested that the atomization efficiency (= liquid atomized / liquid supplied \* 100%) decreased as  $P_L$  decreased after the generation rate reached its maximum value. The maximum aerosol generation rate (~95 mg/min) was only about 20% higher than the aerosol generation rate (~80 mg/min from Figure 4-2) produced by the spray nozzle #30609-2 alone at the same operating conditions in the 10-inch PVC generation chamber. It suggested that the droplet loss was significant due to impaction on the wall of a smaller chamber and droplet interactions between the spray nozzles.

#### Nozzle #30609-5

The Delavan simplex nozzle #30609-5 was next selected and tested in the search for a suitable spray nozzle which could produce at least the same quantity of aerosol mass as nozzle #30609-2 without using the dilution air 1 in the 6-inch diameter generation chamber. It was necessary to find the optimum operating conditions of this spray nozzle so that these could produce maximum aerosol generation rate. Two important parameters,  $P_A$  and  $P_L$ , were evaluated based on the previous tests using 9% sodium chloride solutions. During the tests, the total air flow was maintained at a constant value so that each test had the same droplet loss due to the gravitational settling.

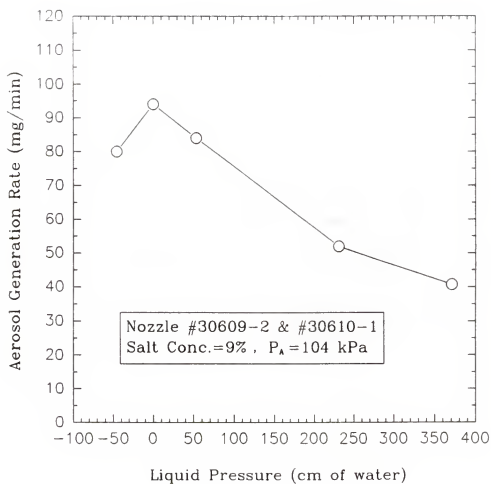


Figure 4-5. Aerosol generation rate as a function of liquid pressure for the Delavan simplex nozzle #30609-2 combined with #30610-1.

Figure 4-6 shows the aerosol generation rate,  $Ma$ , of 9% (by volume) sodium chloride solution as a function of  $P_A$  at  $P_L = -40$  cm of water (-3.9 kPa relative to the ambient pressure). The generation rate was measured by total filtration of solid sodium chloride particles. It was clearly shown that the optimum  $P_A$  value was around 200 kPa. Figure 4-7 displays the liquid flow rate,  $Q_L$ , and aerosol generation rate as a function of  $P_L$  value at  $P_A = 207$  kPa. The  $Q_L$  value increased as the  $P_L$  increased, but the  $Ma$  value decreased as the  $P_L$  was increased after it reached its maximum value of around 110 mg/min. The optimum  $P_L$  value was about negative 40 cm of water.

Figure 4-8 shows the particle size distributions produced by the spray nozzle #30609-5 operated at the selected operating condition ( $P_A = 207$  kPa and  $P_L = -40$  cm of water) using 9% NaCl solution. The MMAD and GSD were 1.84  $\mu\text{m}$  and 1.97, respectively. The liquid aerosol (leaving the generation chamber) was calculated to have a MMAD, GSD, and  $Ma$  of about 4  $\mu\text{m}$ , 2, and 0.6 g/min, respectively. The aerosol had a very broad size distribution. This spray nozzle was selected and employed in the high-output, size-selective aerosol generator. It was operated at  $P_A = 207$  kPa and  $P_L = -40$  cm of water for the rest of the experiments. The nebulizing air flow rate and liquid flow rate were 47.0 lpm and 2.15 lph, respectively.

### Performance of the High-Output, Size-Selective Aerosol Generator

#### Number Distribution Versus Mass Distribution

The APS determines the particle size distribution from the number of particles counted in each size channel. If the particle density is known, the mass distributions can



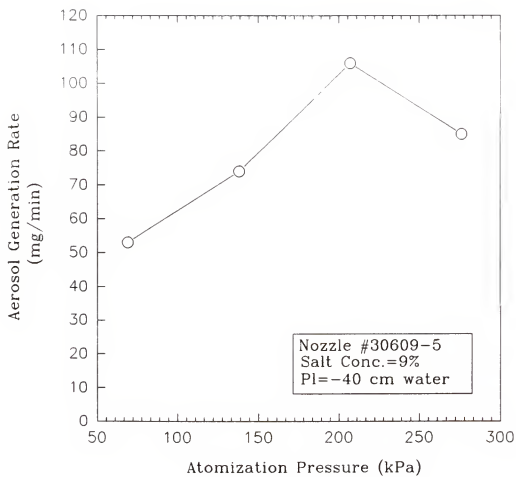


Figure 4-6. Aerosol generation rate as a function of atomization pressure for the Delavan simplex nozzle #30609-5.

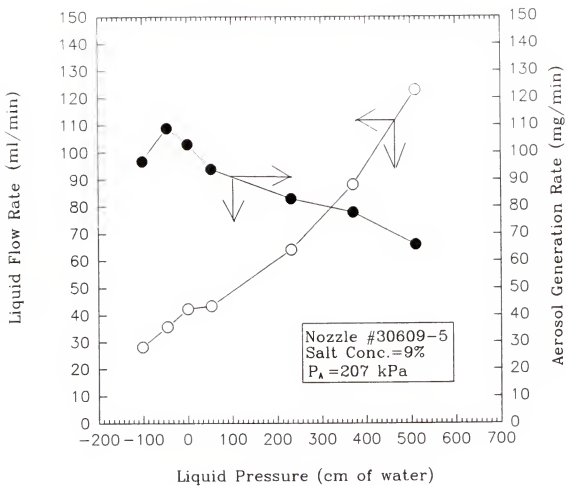


Figure 4-7. Liquid flow rate and aerosol generation rate as a function of liquid pressure for the Delavan simplex nozzle #30609-5.

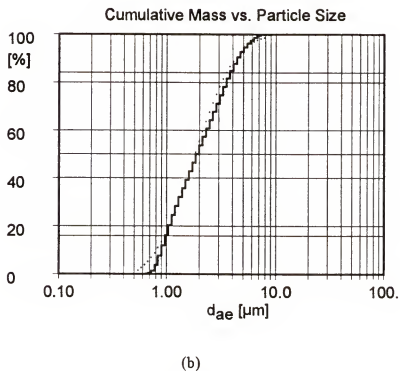
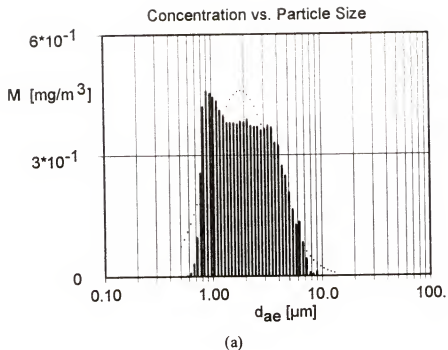
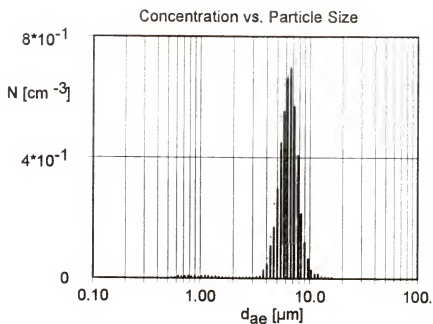


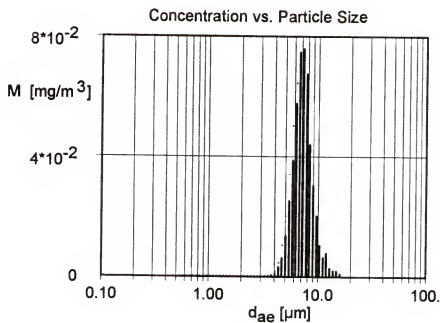
Figure 4-8. Particle size distributions produced by the simplex nozzle #30609-5 at the optimum condition ( $P_A=207$  kPa and  $P_L=-40$  cm of water).  
 a) Mass histogram; b) Mass cumulative curve.

be obtained by converting particle number to mass for each channel. If the number distribution is a perfect log-normal distribution, the converted mass distribution should also be a perfect log-normal distribution and follow the Hatch-Choate equations (Hinds, 1982). Most atomizers generate a high concentration of small particles which are below the APS lower size detection limit. As a result, the number distribution measured by the APS is usually incomplete and small particles create significant phantom counts as previously explained. These two synergistic problems often make the conversion of APS data from number to mass unreliable.

In our aerosol generator, an improved virtual impactor was employed to remove droplets with aerodynamic diameters less than the cut-point size. If the removal efficiency was 100% (no fine particle contamination) and the cut-point size was selected so that the solid particles were all above the lower detection limit, then the number distribution measured by the APS would be complete and the phantom count error would be eliminated. In this case, we had a chance to test the conversion from number to mass for the APS data. Figure 4-9 shows the histogram of the number distribution,  $N$ , and the converted mass distribution,  $M$ , of one APS measurement with nearly no fine particle contamination. The dotted line shows the log-normal fitted curve. The NMAD and GSD values of the number distribution were  $6.17\ \mu\text{m}$  and 1.21, respectively. The MMAD value was  $6.88\ \mu\text{m}$  using the Hatch-Choate equation and  $6.89\ \mu\text{m}$  by log-normal fitting on the converted mass distribution. The GSD value of the mass distribution was 1.21 by log-normal fitting, which was exactly the same as the GSD value of the number distribution. The agreement was excellent and the data showed nearly a perfect log-



(a)



(b)

Figure 4-9. Particle concentration histograms generated by the aerosol generator with virtual impactor  $W = 10 \text{ mm}$ . (no fine particle contamination).  
 a) Number histogram; b) Mass histogram.

normal distribution. Figure 4-10 demonstrates another APS measurement of the particle size distribution with almost no fine particle contamination. The NMAD and GSD values of the number distribution were  $7.16\text{ }\mu\text{m}$  and 1.24, respectively. The MMAD value was  $8.23\text{ }\mu\text{m}$  using the Hatch-Choate equation and  $8.21\text{ }\mu\text{m}$  by log-normal fitting on the converted mass distribution. The GSD of the mass distribution was again shown to have the same value as the number distribution based on the result of log-normal fitting.

If the improved virtual impactor did not completely remove droplets with diameters less than the cut-point size, there would be a significant amount of small particles (fine particle contamination) appearing in the left hand side of the number distribution. This made the log-normal fitting of the number distribution questionable as shown in Figure 4-11(a) which had a NMAD of  $6.51\text{ }\mu\text{m}$  and GSD of 1.73. But if we fitted a log-normal distribution to the converted mass distribution, the mass of fine particles was usually negligible and the fitted result was much more reliable as shown in Figure 4-11(b) with the MMAD =  $8.13\text{ }\mu\text{m}$  and GSD = 1.28. Figure 4-12 demonstrates another extreme example of this situation. The major concern of this project was that particle mass distribution be determined and reported, therefore, the rest of the experimental results are presented based on mass distribution.

#### Particle loss in the TSI Dilutor

The TSI dilutor is provided as an additional option for the APS to reduce particle coincidence problems. Particle penetration efficiency curves are measured by the factory and provided as part of the software to correct size distributions. The penetration

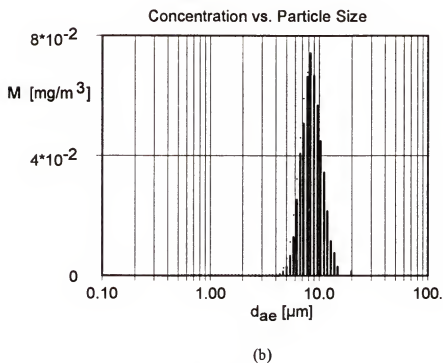
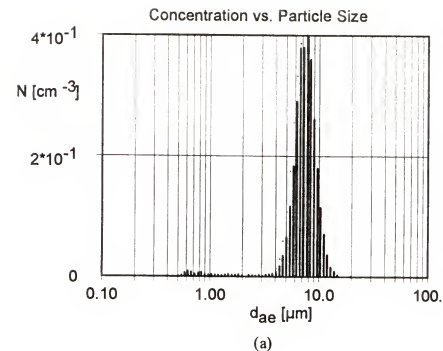
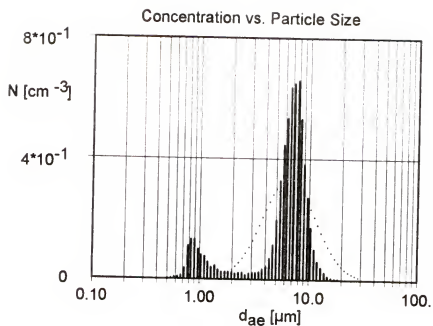
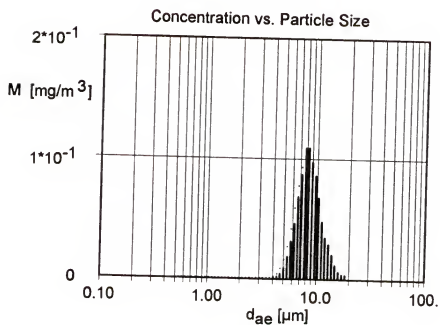


Figure 4-10. Particle concentration histograms generated by the aerosol generator with virtual impactor  $W = 15 \text{ mm}$ . (no fine particle contamination).  
 a) Number histogram; b) Mass histogram.



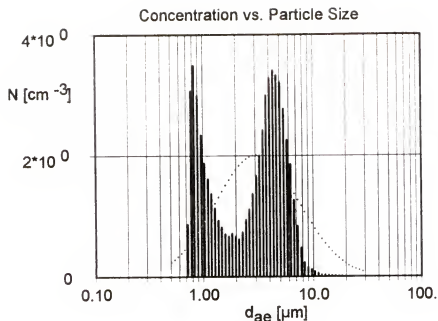
(a)



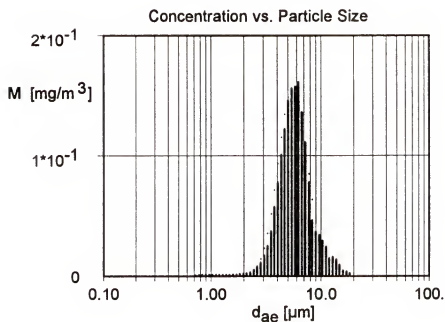
(b)

Figure 4-11. Particle concentration histograms generated by the aerosol generator with virtual impactor  $W = 15 \text{ mm}$ . (with fine particle contamination).  
a) Number histogram; b) Mass histogram.





(a)



(b)

Figure 4-12. Particle concentration histograms generated by the aerosol generator with virtual impactor  $W = 10 \text{ mm}$ . (with fine particle contamination).  
a) Number histogram; b) Mass histogram.

efficiency reduces to about 50% as particle sizes increase to 15  $\mu\text{m}$ . Corrections of this magnitude often make the data in the larger-particle channels unreliable.

An experiment was carried out to study the overall effect on particle size distributions due to particle loss in the dilutor. Figure 4-13(a) shows the particle size distribution measured by the APS with the TSI dilutor. Although the data was corrected by the penetration efficiency curves provided in the software, the particle size distribution was incomplete due to the fact that there were no particles larger than about 10  $\mu\text{m}$  appearing in the size distribution curve (an unusual, sharp cut near 10  $\mu\text{m}$ ). Most of the large particles were lost in the dilutor and were not properly corrected for by the software due to the insignificant number of particles counted (not statistically significant). The aerosol had a MMAD of 4.74  $\mu\text{m}$  and GSD of 1.41 based on log-normal curve-fitting.

The same aerosol was measured by the APS without the TSI dilutor. Figure 4-13(b) shows the result of this measurement. It had a smooth size distribution curve (no sharp cut). Particles up to about 22  $\mu\text{m}$  were measured by the APS and appeared in the size distribution curve. The aerosol had a MMAD of 4.88  $\mu\text{m}$  and GSD of 1.38, which was not significantly different from the previous aerosol. Although the overall effect on the particle size distribution was insignificant with or without the TSI dilutor, the size distribution curve was more complete using the APS without the TSI dilutor. When the APS was used without the TSI dilutor, particle number concentration need to be low ( $\leq 100$  particle/ $\text{cm}^3$  recommended by the manufacture) so that the coincidence error would be minimal. In this study, the particle concentration generated by the aerosol generator could be maintained at an acceptable level through the use of improved virtual impactors

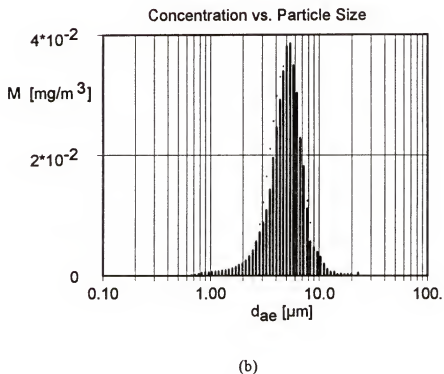
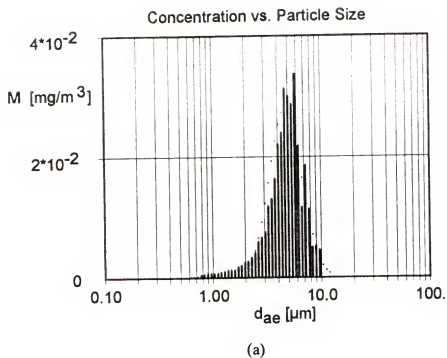


Figure 4-13. Particle size distributions measured by the APS.  
a) With the TSI dilutor; b) Without the TSI dilutor.

and a simple dilution system. So the rest of the particle size measurements were completed without using the TSI dilutor.

#### System Stability and Repeatability

The aerosol generator was operated at one set of fixed conditions ( $Q_t=62.0$  lpm,  $Q_a=2.7$  lpm,  $Q_w=59.3$  lpm,  $Q_c=15.0$  lpm,  $Q_n=47.0$  lpm,  $P_A=207$  kPa, and  $P_L=-40$  cm of water) using 9% NaCl solutions. Three sets of data were collected to test system stability and repeatability. The system was completely turned off after collecting one data set and turned on again to collect another data set. Each data set had four continuous APS measurements of particle size distribution and one single measurement of aerosol generation rate. The sample times were two and ten minutes for each APS and generation rate measurement, respectively.

Table 4-1 shows the values of MMAD, GSD, and Ma for the data sets in these experiments. For the MMAD and GSD values, the standard deviation (STD) was fairly low (less than 3% of average values). The STD value of aerosol generation rate was 11.5% of the average value. The system stability and repeatability were considered to be satisfactory. The slight increase of the aerosol generation rate from data set I to set III was due to the pressure drop increase through the major flow filter which caused the major flow,  $Q_w$ , to decrease during the sampling period. This effect also slightly reduced the MMAD value from run #1 to #12 due to the increase in fine particle contamination in the minor flow,  $Q_a$ .

Table 4-1. MMAD, GSD, and Ma of three data sets used to evaluate the system stability and repeatability.

Data Set	Run #	MMAD ( $\mu\text{m}$ )	GSD	Ma (mg/min)
I	1	6.99	1.28	9.1
	2	6.97	1.29	
	3	6.94	1.27	
	4	6.86	1.28	
II	5	6.64	1.26	11.6
	6	6.64	1.33	
	7	6.67	1.32	
	8	6.55	1.33	
III	9	6.57	1.26	11.9
	10	6.55	1.27	
	11	6.58	1.29	
	12	6.51	1.32	
Average		6.71	1.29	10.9
STD (%)		2.58	1.97	11.5

### Statistics of Particle Counts

In order to have statistically meaningful data, the APS must count a significant number of particles in each size range of interest. If the particle count,  $N_p$ , is low, then the size distribution data is not complete and the log-normal fitting is unreliable. This problem is usually more severe for larger particles due to the fact that there are frequently less particles counted by the APS in large particle size channels. A series of tests were carried out to investigate the size distribution shape change due to the variation of the particle count, as shown in Figure 4-14 and Figure 4-15. The shape of the distribution curve became smoother (more log-normal) as the particle count increased from 181 to 4622. The saw shape of the particle size distribution in Figure 4-14(a) usually indicates that the particle count is too small to be statistically meaningful. The abrupt cut around  $17\ \mu\text{m}$  in Figure 4-14(b) normally implies that particles larger than  $17\ \mu\text{m}$  are either lost by some removal mechanisms or not significantly counted. For this case, several thousand particles needed to be counted in order to obtain reliable log-normal fitting data.

### Effects of the Clean Air Tube Distance and Diameter

A series of tests were carried out to investigate the effect of the clean air tube distance,  $Sc$ , and tube diameter,  $Wc$ , on the size distributions of the generated aerosols. The improved virtual impactor (set I with  $W=10\ \text{mm}$ ) was operated at flows of  $Q_t=62.0\ \text{lpm}$  ( $Q_c=15.0\ \text{lpm}$  and  $Q_n=47.0\ \text{lpm}$ ),  $Q_a=2.7\ \text{lpm}$ , and  $Q_w=59.3\ \text{lpm}$ . The spray nozzle

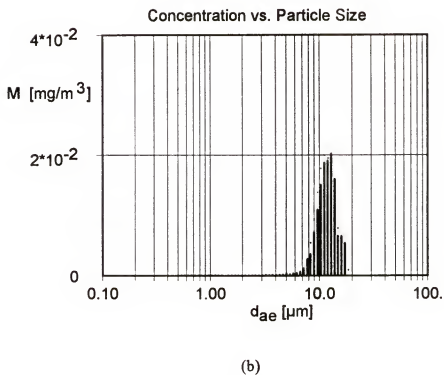
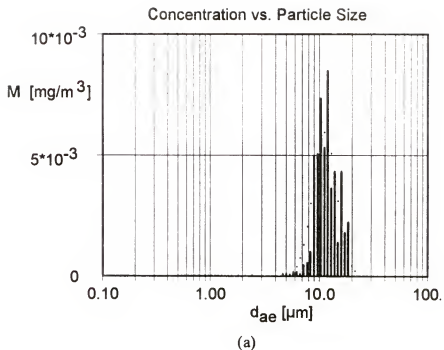
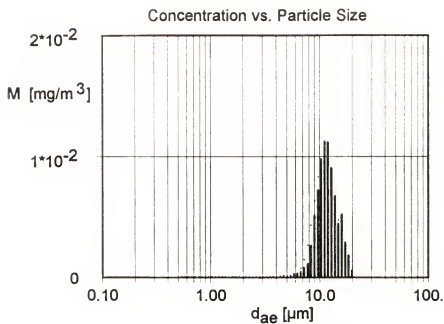
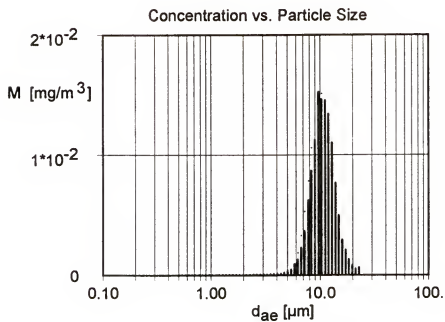


Figure 4-14. Shape change of particle mass concentration histograms due to the variation of particle count,  $N_p$ .  
 a)  $N_p=181$ ; b)  $N_p=781$ .



(a)



(b)

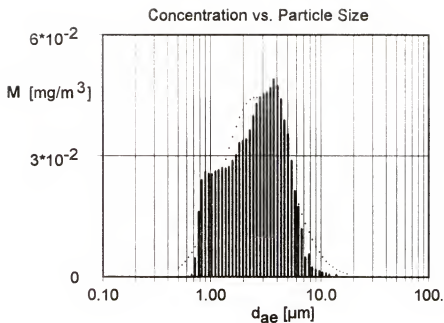
Figure 4-15. Shape change of particle mass concentration histograms due to the variation of particle count,  $N_p$ .

a)  $N_p=1251$ ; b)  $N_p=4622$ .

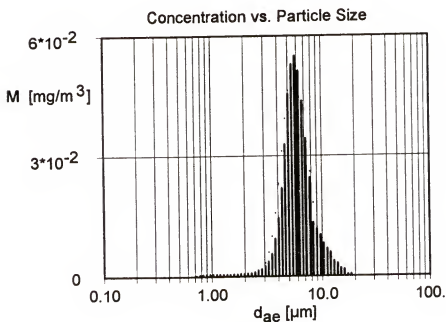


was operated at its optimum condition using 9% NaCl solutions. Figure 4-16 and Figure 4-17 show the particle mass concentration histograms obtained at different Sc values with the same Wc value of 14 mm. At Sc=10 mm, the MMAD and GSD were 2.55  $\mu\text{m}$  and 1.95, respectively. Apparently, the improved virtual impactor was not working correctly. This deficiency was due to the fact that the clean air tube was so close to the inlet of the acceleration nozzle that it caused the air flow to become non-uniform and, therefore, the particle separation efficiency was dramatically decreased. As the Sc value was increased to 20 mm, the particle separation efficiency was greatly improved and the aerosol had MMAD, GSD, and Ma values of 5.70  $\mu\text{m}$ , 1.30, and 4.9 mg/min, respectively. As the Sc value was further increased to 40 mm, the MMAD and GSD did not significantly change (MMAD=5.88  $\mu\text{m}$  and GSD=1.34) but the Ma value was increased to 11.4 mg/min. The Sc value was finally increased to 60 mm. While the MMAD and GSD did not have notable variation, the Ma value was slightly reduced to 9.3 mg/min. From the above test results, the particle loss would be a minimum as the Sc was set to 40 mm due to the fact that it had the highest aerosol generation rate.

The clean air tube diameter was next increased to see if further improvements in the particle separation efficiency could be made. Figure 4-18 displays the particle number and mass concentration histograms obtained with the Sc and Wc values of 45 mm and 22 mm, respectively. It was clearly demonstrated that particles less than the cutpoint diameter were totally removed based on either number or mass distribution and, therefore, there was no fine particle contamination at this operating condition. The aerosol distribution had MMAD, GSD, and Ma values of 6.86  $\mu\text{m}$ , 1.18, and 8.6 mg/min,

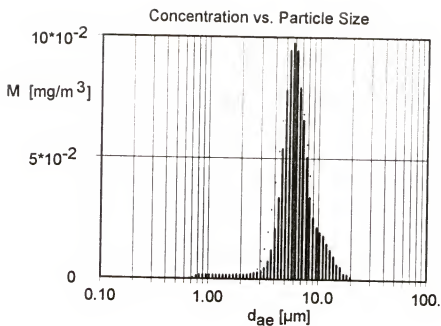


(a)

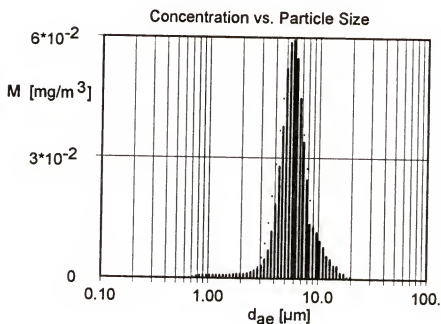


(b)

Figure 4-16. Particle mass concentration histograms obtained with different clean air tube distances,  $Sc$  (tube diameter,  $W_c$ , = 14 mm).  
a)  $Sc=10$  mm; b)  $Sc=20$  mm.



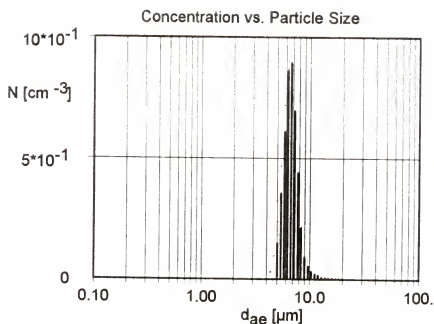
(a)



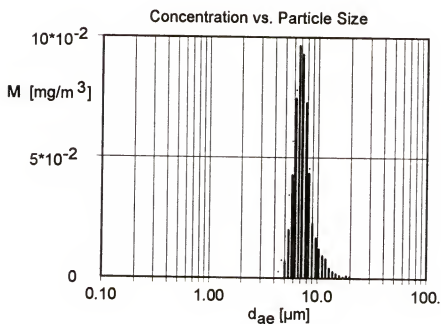
(b)

Figure 4-17. Particle mass concentration histograms obtained with different clean air tube distances,  $Sc$  (tube diameter,  $W_c = 14$  mm).

a)  $Sc=40$  mm; b)  $Sc=60$  mm.



(a)



(b)

Figure 4-18. Particle concentration histograms obtained with the clean air tube distance,  $Sc$ , and tube diameter,  $Wc$ , of 45 mm and 22 mm, respectively.  
a) Number histogram; b) Mass histogram.

respectively. Two sets of improved virtual impactors ( $W=10$  mm and  $W=15$  mm) were employed in the aerosol generator. To simplify the operation of the aerosol generator, the clean air tube with  $W_c=22$  mm was installed for both sets and the tube distance,  $Sc$ , was fixed at 45 mm for one set ( $W=10$  mm) and 35 mm for another set ( $W=15$  mm).

### Generation of Narrowly Size-Distributed Aerosols

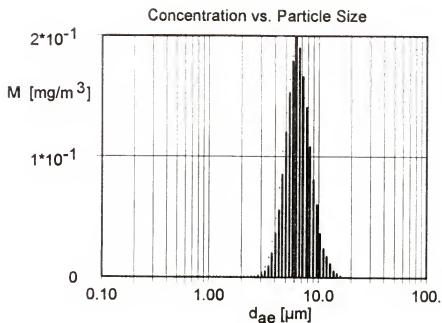
#### Operating conditions #1 and #2

Two sets of basic operating conditions were used to generate particles with narrow size distributions. Table 4-2 lists the operating conditions of the improved virtual impactor and the aerosol outputs using a 9% sodium chloride solution as the Delavan spray nozzle was operated at  $P_A=207$  kPa and  $P_L=-40$  cm of water. In operating condition set #1, the virtual impactor set I was operated at flows of  $Q_t=62.0$  lpm ( $Q_c=15.0$  lpm and  $Q_n=47$  lpm),  $Q_w=53.7$  lpm, and  $Q_a=8.3$  lpm. The nozzle air velocity and Reynolds number of the virtual impactor were calculated to be 1,300 cm/sec and 8,700, respectively. The virtual impactor has been shown (Chen et al., 1985 and Chein and Lundgren, 1993) to be able to maintain a clean air core in the center of the aerosol flow without distortion at such a high Reynolds number.

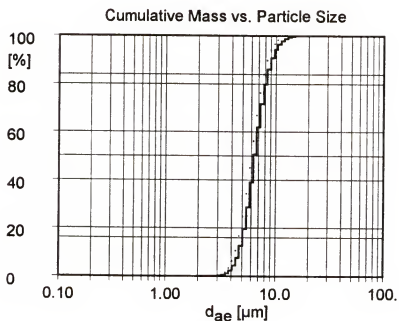
Figure 4-19 shows the mass concentration histogram and cumulative curve of the generated aerosol which had a MMAD, GSD, and Ma of 6.23  $\mu\text{m}$ , 1.29, and 23.8 mg/min, respectively. The mass concentration histogram indicated that the generated aerosol had a very smooth and narrow distribution curve. The improved virtual impactor was separating particles so efficiently that there were almost no fine particles below 3  $\mu\text{m}$

Table 4-2. Two sets of basic operating conditions and the corresponding aerosol outputs using a 9% sodium chloride solution (the Delavan spray nozzle was operated at  $P_A=207$  kPa and  $P_L=-40$  cm of water).

SET#	Virtual Impactor Conditions					Aerosols			Number Needed to produce 225 mg/min
	W (mm)	Qt (lpm)	Qc (lpm)	Qw (lpm)	Qa (lpm)	MMAD ( $\mu$ m)	GSD	Ma (mg/min)	
1	10	62.0	15.0	53.7	8.3	6.23	1.29	23.8	10
2	15	74.0	27.0	60.4	13.6	8.21	1.24	14.1	16



(a)



(b)

Figure 4-19. Particle mass concentration distributions using 9% sodium chloride solution at operating condition set #1.

a) Mass histogram; b) Mass cumulative curve.

appearing in the mass distribution curve in spite of a relatively high minor flow ratio ( $= Q_a/Q_t * 100\%$ ) of 13.4%. The improved virtual impactor had to remove small particles completely for the HOSSAG to generate particles with narrow size distributions due to the fact that the spray nozzle produced a tremendous number of fine particles. During the tests of the HOSSAG, it was found that an aerosol with a GSD as high as 1.8 could be produced if the improved virtual impactor was operated without the central clean air flow or with the clean air flow distorted or contaminated with aerosols. The dotted line, which was shown on both mass concentration histogram and cumulative curve, showed that the aerosol size distribution curve was nearly log-normal. The aerosol had such a high mass generation rate, 23.8 mg/min, that only ten aerosol generators would be needed to meet the requirement of the maximum mass flow rate, 225 mg/min, for the human exposure chamber.

The operating condition set #2 had the same condition for the spray nozzle and sodium chloride solution, but the virtual impactor set II was used instead of set I and operated at flows of  $Q_t=74.0$  lpm, ( $Q_c=27.0$  lpm and  $Q_n=47.0$  lpm),  $Q_w=60.4$  lpm, and  $Q_a=13.6$  lpm. The nozzle air velocity and Reynolds number of the virtual impactor were calculated to be 700 cm/sec and 7,000, respectively. With a larger nozzle diameter of 15 mm, the cutpoint diameter was increased and, therefore, more small particles were removed. The generated aerosol was expected to have a larger MMAD and smaller GSD. While the minor flow ratio was set at a fairly high value of 18.4% to increase the mass generation rate, the clean air flow rate was maintained at about two times the minor flow rate to minimize the fine particle contamination. This is the ratio recommended by Chen



et al., 1985, based on their studies of an improved virtual impactor. Figure 4-20 displays the mass concentration histogram and cumulative distribution curve of the generated aerosol with a MMAD, GSD, and Ma of 8.21  $\mu\text{m}$ , 1.24, and 14.1 mg/min, respectively. Both the mass concentration histogram and cumulative curve indicated that the aerosol had a very smooth and narrow size distribution curve and the log-normal fitting result was excellent. The mass generation rate was decreased mainly due to the increase of the cutpoint diameter. Sixteen generators would be required to achieve the maximum aerosol mass flow rate.

#### Changing solution concentrations

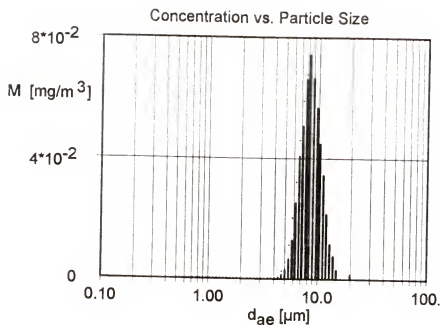
The size of solid particles can be varied by changing the solution concentration,  $F_v$ , of the same droplets selected by the improved virtual impactor. The following equations could be used to convert from droplet diameter,  $d_d$ , to equivalent volume diameter of solid particle,  $d_s$ , and from equivalent volume diameter to aerodynamic diameter:

$$d_s = d_d (F_v)^{1/3} \quad (4-1)$$

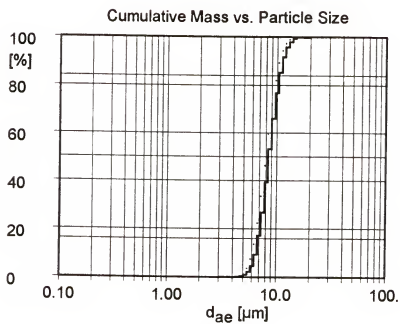
and

$$d_{ae} = d_s \left[ \rho_p C_s / (\rho_0 \chi C_{sc}) \right]^{1/2} \quad (4-2)$$

where  $C_s$  and  $C_{sc}$  are Cunningham correction factors for equivalent volume diameter and aerodynamic diameter, respectively. If the equivalent volume diameter of the solid



(a)



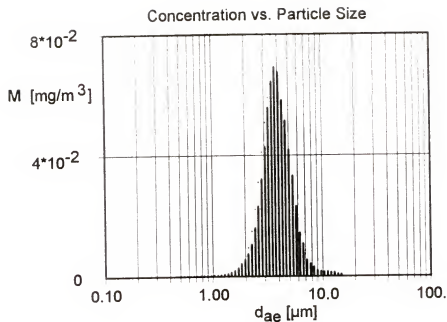
(b)

Figure 4-20. Particle mass concentration distributions using 9% sodium chloride solution at operating condition set #2.

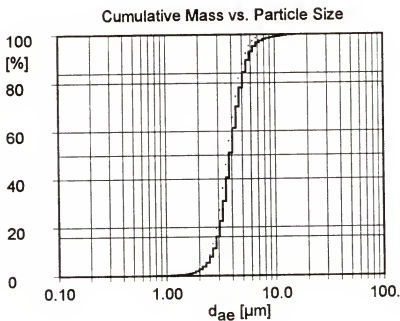
a) Mass histogram; b) Mass cumulative curve.

particle is obtained from Equation 4-1, then the aerodynamic diameter could be calculated from Equation 4-2. Alternatively, the original droplet diameter could be calculated if the aerodynamic diameter of the final particle is known. Based on the results of the operating condition set #1, Equation 4-1 and 4-2, the original aerosol (droplets) selected by the improved virtual impactor was calculated to have a MMAD of 9.73  $\mu\text{m}$ , GSD of 1.29, and Ma of 120 mg/min. Similar calculations were performed for the operating condition #2. The original aerosol selected by the improved virtual impactor had a MMAD of 12.8  $\mu\text{m}$ , GSD of 1.24, and Ma of 71 mg/min.

Figure 4-21 and Figure 4-22 demonstrate the mass distribution and cumulative curves of an aerosol obtained by reducing the sodium chloride solution to 1% and 0.05% (by volume) using operating condition set #1. For the 1% solution, the aerosol had the MMAD, GSD, and Ma of 3.75  $\mu\text{m}$ , 1.33, and 3.79 mg/min, respectively. The MMAD value was 1.25 times of the theoretical value (3.00  $\mu\text{m}$ ) based on the solution concentration ratio. However, Matteson and Stober (1967) showed experimentally that the particle diameter varies with the 0.28 power rather than the theoretical 1/3 power for sodium chloride. If their results were applied, the MMAD value would be only 1.11 times the expected value (3.37  $\mu\text{m}$ ). This agreement was considered to be satisfactory in such a complicated measurement system. While the GSD difference was insignificant (1.29 vs. 1.33) which was expected, the Ma ratio was 6.3, rather than the expected ratio of 9 (solution concentration ratio). For the 0.05% solution, the aerosol had the MMAD, GSD, and Ma of 1.38  $\mu\text{m}$ , 1.46, and 0.21 mg/min, respectively. At such low solution concentrations, droplets might evaporate during the acceleration process in the virtual



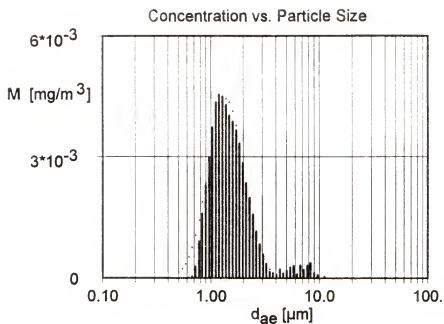
(a)



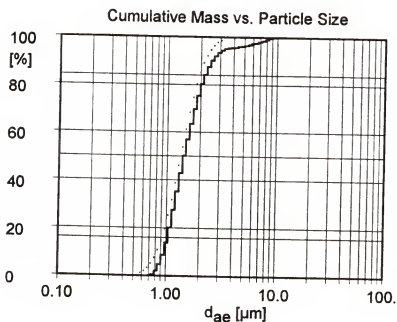
(b)

Figure 4-21. Particle mass concentration distributions using 1% sodium chloride solution at operating condition set #1.

a) Mass histogram; b) Mass cumulative curve.



(a)



(b)

Figure 4-22. Particle mass concentration distributions using 0.05% sodium chloride solution at operating condition set #1.

a) Mass histogram; b) Mass cumulative curve.

impactor, which decreased original droplet sizes. In addition, there were a significant number of particles below the APS lower detection limit. These two reasons complicated the comparison between experimental data and theoretical values. A theoretical calculation was carried out to estimate salt concentrations and number of generators needed to produce the mass flow rate of 225 mg/min as a function of particle aerodynamic diameter. Figure 4-23 shows the theoretical relationship (solid line) and also displays experimental data (hollow circle for salt concentrations and solid circle for number of generator). The aerosol MMAD decreased to 1.38  $\mu\text{m}$  as the sodium chloride solution was reduced to 0.05% based on the experimental data. But the aerosol generation rate was too low (0.21 mg/min) to achieve the maximum aerosol mass flow rate realistically.

#### Changing the minor flow rate

The aerosol output was highly affected by the minor flow rate of the improved virtual impactor. As the minor flow rate decreased, the amount of small particles following the minor flow was reduced and, therefore, the aerosol had a larger MMAD, smaller GSD, and lower Ma.

Figure 4-24 shows the mass concentration histogram and cumulative curve of the aerosol generated from operating condition set #2 but the minor flow rate was reduced from 13.6 to 4.3 lpm. This aerosol had the MMAD of 9.99  $\mu\text{m}$ , GSD of 1.21, and Ma of 1.72 mg/min. The aerosol generation rate was significantly reduced from 14.1 to 1.72 mg/min as the minor flow rate decreased from 13.6 to 4.3 lpm. It would require an

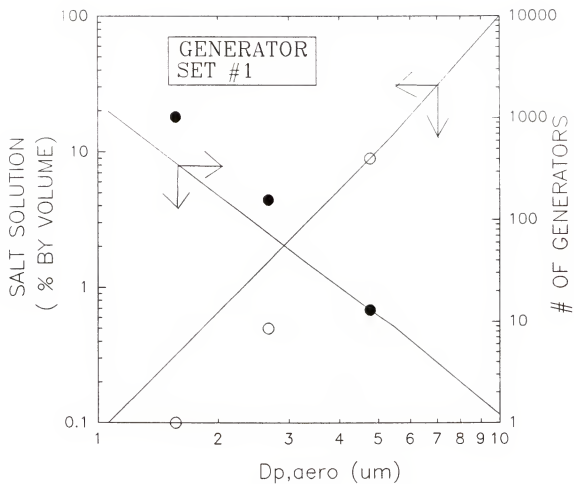
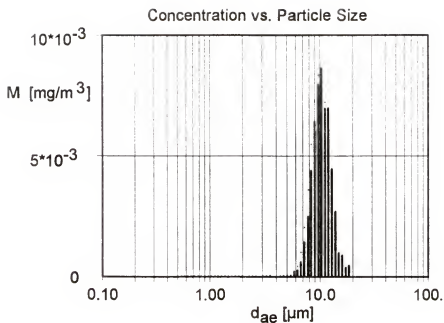
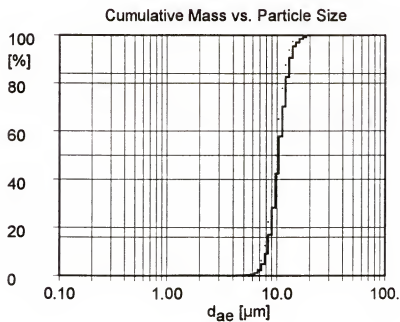


Figure 4-23. Salt concentration and number of generators as a function of particle aerodynamic diameter based on operating condition set #1 (solid line for theoretical calculation and circle points for experimental data).



(a)



(b)

Figure 4-24. Particle mass concentration distributions obtained with operating condition set #2 but minor flow rate=4.3 lpm.

a) Mass histogram; b) Mass cumulative curve.



unpractical number of generators, 131, to achieve the mass flow rate of 225 mg/min at this operating condition.

## CHAPTER 5 CONCLUSIONS

### Testing of Delavan Simplex Nozzles

Three combinations of simplex nozzles were tested. A Delavan simplex nozzle #30609-5 installed on the bottom of the 6-inch diameter generation chamber was found to be most suitable for droplet generation. The effect of atomization pressure and liquid pressure on the droplet generation was investigated using a 9% (by volume) sodium chloride solution. Test results indicated the aerosol generation rate,  $\dot{M}_a$ , reached a maximum value of 110 mg/min as the atomization pressure and liquid pressure were equal to 207 kPa and negative 3.9 kPa (relative to the ambient pressure), respectively. At these operating conditions, the nebulizing air flow rate and liquid flow rate were measured to be 47 lpm and 2.15 lph, respectively. Measurements of particle size distributions were performed on the resulting solid particles of sodium chloride. The aerosol generated from a 9% NaCl solution had a mass median aerodynamic diameter, MMAD, of 1.84  $\mu\text{m}$  and geometric standard deviation, GSD, of 1.97 as the spray nozzle was set at the selected operating conditions. In addition, there was a significant amount of submicron particles not being measured by the Aerodynamic Particle Sizer due to the lower detection limit ( $\sim 0.8 \mu\text{m}$ ) of the instrument.

### Performance of the High-Output, Size-Selective Aerosol Generator

A high-output, size-selective aerosol generator was designed and built to produce water-soluble test aerosols for the EPA human exposure laboratory, located on the campus of the University of North Carolina at Chapel Hill. Droplet generation was performed by the Delavan simplex nozzle #30609-5. An improved clean air core virtual impactor was employed to segregate particles according to their aerodynamic diameter. The improved virtual impactor was demonstrated to separate out droplets with aerodynamic diameter less than the impactor cut-point size very efficiently (close to 100%), producing a nearly perfect log-normal aerosol distribution. The MMAD values obtained by using the Hatch-Choate equation and by log-normal fitting of the mass distribution data agreed extremely well.

The effect of particle losses within the TSI dilutor on particle size distributions was investigated. The data showed that many of the large particles ( $> 10 \mu\text{m}$ ) were lost in the dilutor and were not properly corrected for by the software due to an insignificant number of particles counted. The size distribution curve was more complete using the Aerodynamic Particle Sizer without the dilutor. However, the overall effect on the MMAD and GSD values was not significant with or without the dilutor.

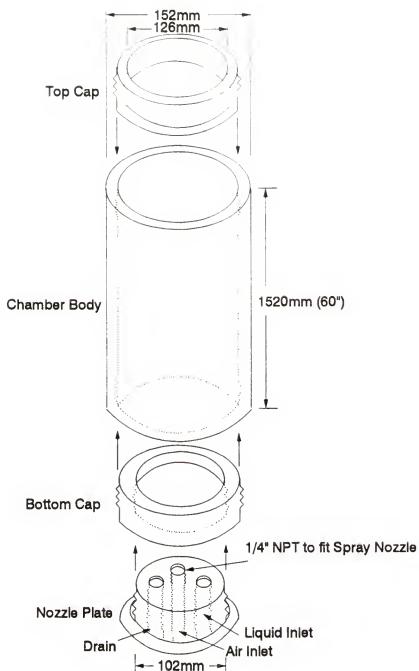
A high particle count was found to be very important for the Aerodynamic Particle Sizer to obtain statistically meaningful data. Several thousand particles were needed to be counted in order to obtain reliable log-normal fitting data.

Four different values of the clean air tube distance,  $Sc$ , were investigated to study the effect on the size distributions of generated aerosols for the virtual impactor set I. As the  $Sc$  was set to 10 mm, the aerosol flow became non-uniform and, therefore, the virtual impactor did not fractionate particles efficiently. The generated aerosol had a very broad size distribution curve ( $GSD = 1.95$ ). As the  $Sc$  value was increased to 20 mm, the particle separation efficiency was greatly improved and the aerosol had MMAD, GSD, and Ma values of 5.70  $\mu\text{m}$ , 1.30, and 4.9 mg/min, respectively. Increasing the  $Sc$  value to 40 mm and 60 mm did not change MMAD and GSD values significantly, but the Ma reached its maximum value of 11.4 mg/min at  $Sc = 40$  mm. The clean air tube diameter was next increased to 22 mm as the  $Sc$  was set to 45 mm. Fine particle contamination was totally eliminated in the minor flow and the generated aerosol had MMAD, GSD, and Ma values of 6.86  $\mu\text{m}$ , 1.18, and 8.6 mg/min, respectively.

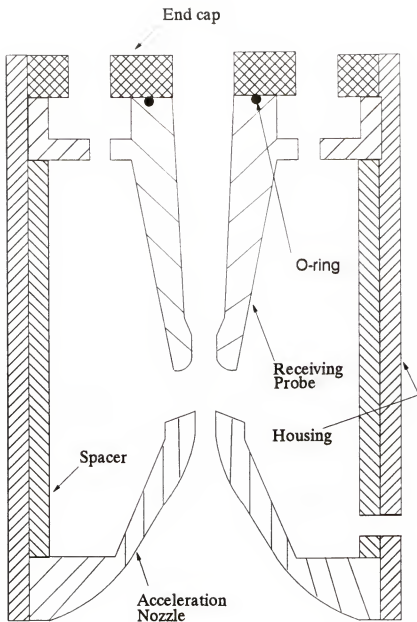
Two sets of basic operating conditions of the aerosol generator were used to generate particles with narrow size distributions. The operating condition #1 generated an aerosol with a MMAD, GSD, and Ma of 6.23  $\mu\text{m}$ , 1.29, and 23.8 mg/min, respectively, from a 9% NaCl solution. With this mass generation rate, only ten aerosol generators would be needed to meet the requirement of the maximum mass flow rate, 225 mg/min, for the EPA human exposure chamber. The operating condition #2 produced an aerosol with a MMAD, GSD, and Ma of 8.21  $\mu\text{m}$ , 1.24, and 14.1 mg/min, respectively, from a 9% NaCl solution. Sixteen generators would be required to achieve the maximum aerosol mass flow rate. Based on these two operating conditions, aerosols with smaller or larger MMADs could be generated by changing either the solution concentration or the minor

flow rate of the improved virtual impactor. The test data showed that the aerosol generator was capable of producing an aerosol with a MMAD value varying from 1.38 to 9.99  $\mu\text{m}$ , a GSD value varying from 1.18 to 1.46, and a Ma value varying from 0.21 to 23.8 mg/min at 0.05% to 9% NaCl solutions. This aerosol generator will satisfy the need for narrowly size-distributed test aerosols in the human exposure chamber. To achieve the maximum aerosol mass flow rate, 225 mg/min, in the exposure chamber, the MMAD of the generated particle has a practical limit to values between 3 and 9  $\mu\text{m}$ .

APPENDIX  
DETAILED DESIGN DRAWINGS OF THE GENERATION CHAMBER,  
THE IMPROVED VIRTUAL IMPACTOR, AND THE CLEAN AIR SECTION.

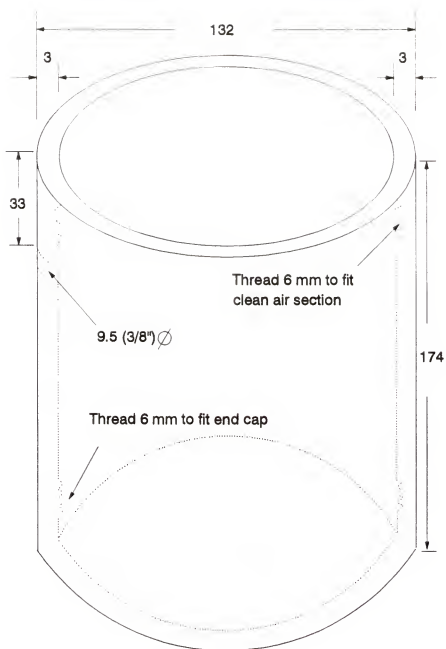


Overall Assembly of	HungMin Chein	Drawing Not on Scale
Aerosol Generation Chamber	May 26, 1994	Dimension: mm
University of Florida	File: chamber.drw	Drawing No: 1 of 1
Environmental Engineering Dept.	Material: polyvinyl chloride (PVC)	

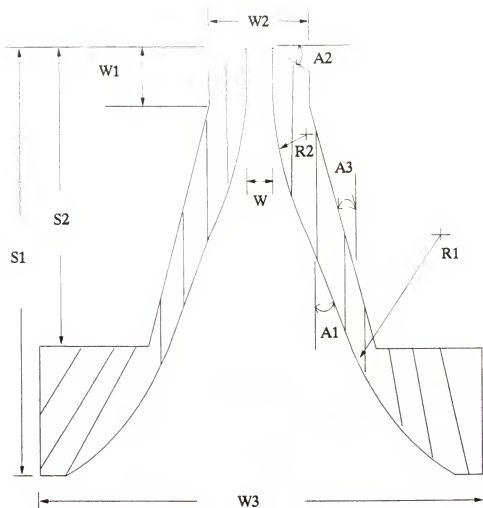


Virtual Impactor	HungMin Chein	Drawing Not on Scale
Part A: Assembly View	May 26, 1994	Dimension: mm
University of Florida	File: viasemb.drw	Drawing No: 1 of 6
Environmental Engineering Dept.	Material: Anodized Aluminum	



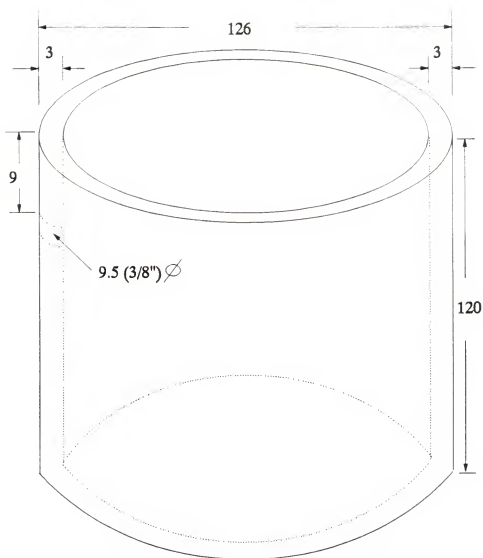


Virtual Impactor	HungMin Chein	Dimension: mm	Tolerance: 0.05mm
Part B: Housing	May 26, 1994	Drawing Not on Scale	
University of Florida		File: vihous.drw	Drawing No: 2 of 6
Environmental Engineering Dept.		Material: Anodized Aluminum	

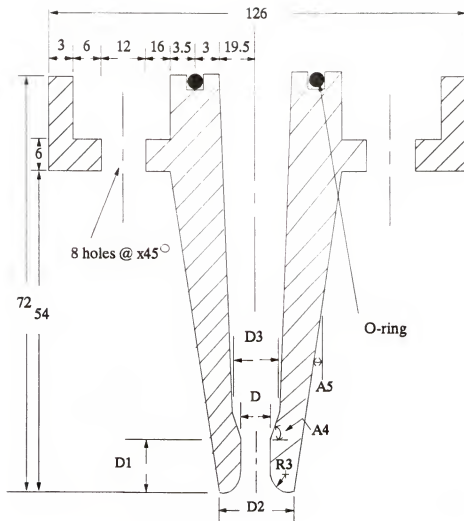


Set	W	W1	W2	W3	S1	S2	A1	A2	A3	R1	R2
I	10.0	10.0	30.0	126.0	74.0	56.0	30°	15°	30°	42.0	2.4
II	15.0	15.0	45.0	126.0	69.0	51.0	30°	15°	30°	49.4	3.6

Virtual Impactor	HungMin Chein	Dimension: mm	Tolerance: 0.05mm
Part C: Nozzle	May 26, 1994	Drawing Not on Scale	
University of Florida		File: vinoz.drw	Drawing No: 3 of 6
Environmental Engineering Dept.		Material: Anodized Aluminum	

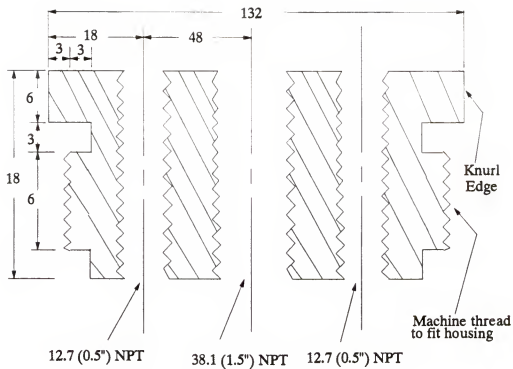


Virtual Impactor	HungMin Chein	Dimension: mm	Tolerance: 0.05mm
Part D: Spacer	May 26, 1994	Drawing Not on Scale	
University of Florida		File: vispacer.drw/Drawing No: 4 of 6	
Environmental Engineering Dept.		Material: Anodized Aluminum	

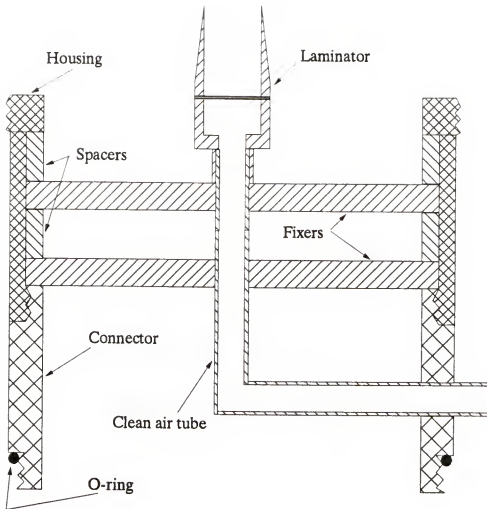


Set	D	D1	D2	D3	A4	A5	R3
I	15.0	10.0	30.0	24.0	45°	15°	3.0
II	22.5	15.0	45.0	28.5	45°	15°	4.5

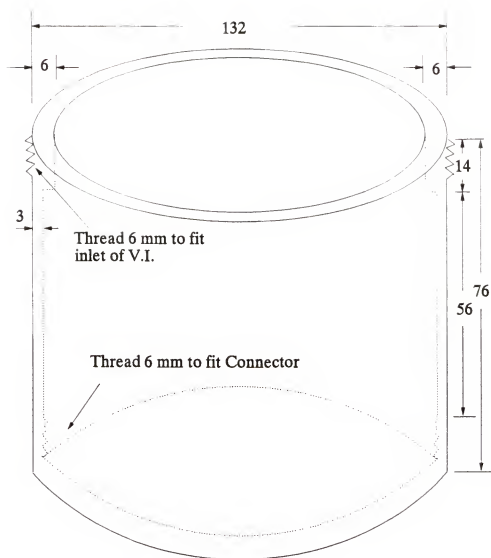
Virtual Impactor	HungMin Chein	Dimension: mm	Tolerance: 0.05mm
Part E: Probe	May 26, 1994	Drawing Not on Scale	
University of Florida		File: viprob.drw	Drawing No: 5 of 6
Environmental Engineering Dept.		Material: Anodized Aluminum	



Virtual Impactor	HungMin Chein	Dimension: mm	Tolerance: 0.05mm
Part F: End Cap	May 26, 1994	Drawing Not on Scale	
University of Florida		File: viendcap.drw	Drawing No: 6 of 6
Environmental Engineering Dept.		Material: Anodized Aluminum	

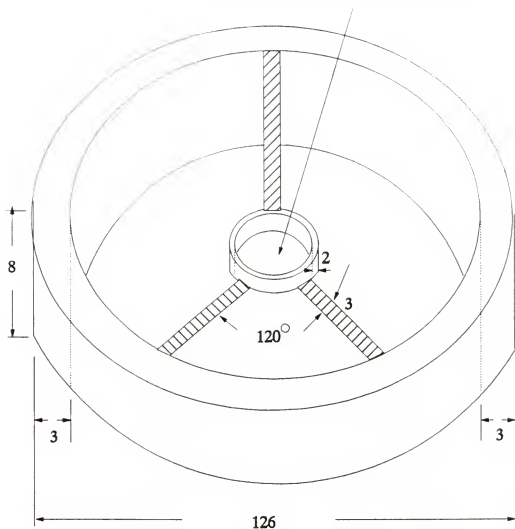


Clean Air Section	HungMin Chein	Dimension: mm	Tolerance: 0.05mm
Part A: Assembly View	May 26, 1994	Drawing Not on Scale	
University of Florida		File: ca.drw	Drawing No: 1 of 6
Environmental Engineering Dept.		Material: Anodized Aluminum	



Clean Air Section	HungMin Chein	Dimension: mm	Tolerance: 0.05mm
Part B: Housing	May 26, 1994	Drawing Not on Scale	
University of Florida		File:cahous.drw	Drawing No: 2 of 6
Environmental Engineering Dept.		Material: Anodized Aluminum	

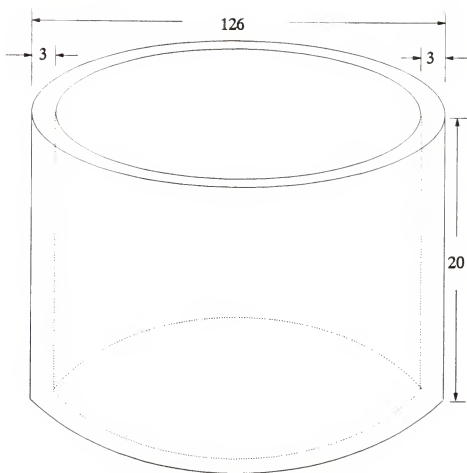
Fit the clean air tube (O.D. = 16mm)



Clean Air Section	HungMin Chein	Dimension: mm	Tolerance: 0.05mm
Part C: Fixer	May 26, 1994	Drawing Not on Scale	
University of Florida		File: caxfixer.drw	Drawing No: 3 of 6
Environmental Engineering Dept.		Material: Anodized Aluminum	

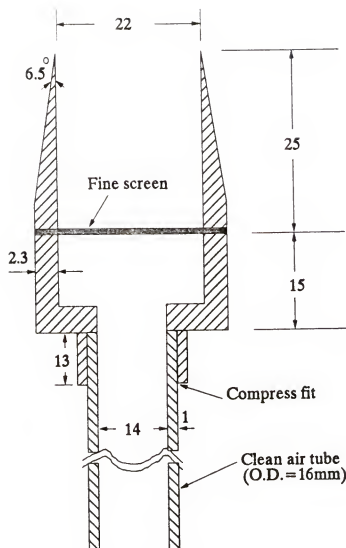
Note: Two fixers required.



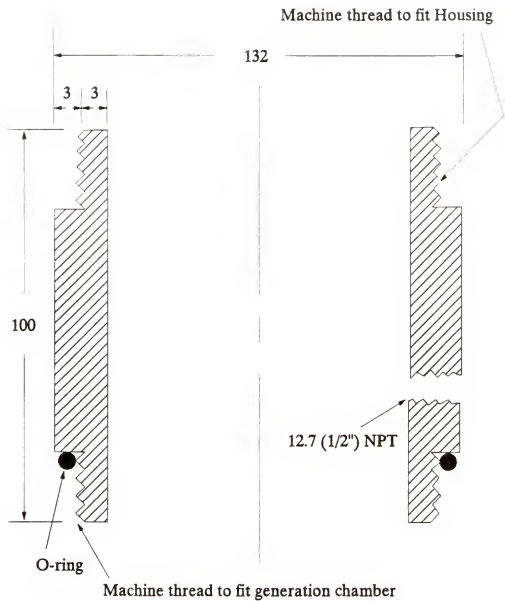


Clean Air Section	HungMin Chein	Dimension: mm	Tolerance: 0.05mm
Part D: Spacer	May 26, 1994	Drawing Not on Scale	
University of Florida		File: caspacer.drw	Drawing No: 4 of 6
Environmental Engineering Dept.		Material: Anodized Aluminum	

Note: Two spacers required.



Clean Air Section	HungMin Chein	Dimension: mm	Tolerance: 0.05mm
Part E: Laminator	May 26, 1994	Drawing Not on Scale	
University of Florida Environmental Engineering Dept.	File: calamina.drw		Drawing No: 5 of 6
	Material: 316 stainless steel		



Clean Air Section	HungMin Chein	Dimension: mm	Tolerance: 0.05mm
Part F: Connector	May 26, 1994	Drawing Not on Scale	
University of Florida		File: caconnec.drw	Drawing No: 6 of 6
Environmental Engineering Dept.		Material: Anodized Aluminum	

## REFERENCE LIST

- Anderson T. L. Charlson, R. J. and Covert D. S. (1993) Aerosol Sci. Technol. 19:317-329.
- Baron, P.A. (1986). Aerosol Sci. Technol. 5:55-67.
- Barr, E.B., Hoover, M.D., Kanapilly, G.M., Yeh, H.C., and Rothenberg, S.J. (1983). Aerosol Sci. Technol. 2:437-442.
- Chen, B.T., and Yeh, H.C. (1987). J. of Aerosol Sci. 18:203-214.
- Chen, B.T., Yeh, H.C., and Cheng, Y.S. (1985). J. of Aerosol Sci. 16:343-354.
- Chen, B.T., Yeh, H.C., and Cheng, Y.S. (1986). Aerosol Sci. Technol. 5:369-376.
- Chen, B.T., Yeh, H.C., and Rivero, M.A. (1988). J. of Aerosol Sci. 19:137-146.
- Chen, H., and Lundgren, D.A. (1993). Aerosol Sci. Technol. 18: 376-388.
- Cheng, Y.S., Chen, B.T., and Yeh, H.C. (1990). J. Aerosol Sci. 21:701-710.
- Cheng, Y.S., Chen, B.T., and Yeh, H.C. (1993). Apply Occup. Environ. Hyg. 8(4):307-312.
- Conner, W.D. (1966). J. Air Pollut. Control Assoc. 1:35-38.
- Forney, L.J., Ravenhall, D.G., and Lee, S.S. (1982). Environ. Sci. Technol. 16:492-497.
- Friedlander, S.K. (1977). Smoke, Dust, and Haze, Wiley, New York.
- Gotsch, O.H. (1994). High-Output Generation and Size-Fractionation of Micron Size Particles, Master's Thesis, University of Florida, Gainesville, FL.
- Hassan, Y.A., Jones, B.G., and Yule, T.J. (1979). Trans. Am. Nuclear Soc. 33:182-184.
- Heitbrink, W.A., Baron, P.A., and Willeke, K. (1991). Aerosol Sci. Technol. 14:112-126.
- Hinds, W.C. (1982). Aerosol Technology. John Wiley and Sons, Inc., New York.

- Hounam, R.F., and Sherwood, R.J. (1965). Am. Ind. Hyg. Assoc. J. 2:122-131.
- Horn, H.G. (1993). A New Technique for Automatic Phantom and Coincidence Count Reduction in the Aerodynamic Particle Sizer APS 3310. Thermo System Inc. report.
- Keskinen, J., Janka, K., and Lehtimäki, M. (1987). Aerosol Sci. Technology. 9:167-176.
- Lefebvre, A.H. (1989). Atomization and Sprays, Hemisphere Publishing Corp., New York.
- Liebhaber, F.B., Lehtimäki, M., and Willeke, K. (1991). Aerosol Sci. Technol. 15:208-213.
- Loo, B.W., and Cork, C.P. (1988). Aerosol Sci. Technol. 9:167-176.
- Loo, B.W., Jaklevic, J.M., and Groulding, F.S. (1976). In Fine Particles (B.Y.H. Liu, ed.), Academic Press Inc., New York, pp. 311-350.
- Marple, V.A., and Chien, C.M. (1980). Environ. Sci. Technol. 14:976-985.
- Marple, V.A., Liu, B.Y.H., and Burton, R.M. (1990). J. Air Waste Manage. Assoc. 40:762-767.
- Marshall, I.A., Mitchell, J.P., and Griffiths, W.D. (1991). J. Aerosol Sci. 22:73-89.
- Masters, K. (1985). Spray Drying Handbook, Halsted Press, New York.
- Masuda, H., Hochrainer, D., and Stober, W. (1979). J. Aerosol Sci. 10:275-287.
- Matteson, M. and Stober, W. (1967). J. Colloid and Interface Sci. 23:203-214.
- McFarland, A.R., Bertch, R.W., Fisher, G.L., and Prentice, B.A. (1977). Environ. Sci. Technol. 11:781-784.
- Noone, K. J., Ogren, J. A., Heintzenberg, J., Charlson, R. J. and Covert D. S. (1988). Aerosol Sci. Technol. 8:235-244.
- Novick, V.J., and Alvarez, J.L. (1987). Aerosol Sci. Technol. 6:63-70.
- Ogren, J. A., Heintzenberg, J., and Charlson, R. J. (1985). Geophys. Res. Lett. 12:121-124.
- Pilacinski, W., Ruuskanen, J., Chen, C.C., Pan, M.J., and Willeke, K. (1990). Aerosol Sci. Technol. 13:450-458.

- Rader, D.J., Brockmann, J.E., Ceman, D.L., and Lucero, D.A. (1990). Aerosol Sci. Technol. 13:514-521.
- Ravenhall, D.G., Forney, L.J., and Hubbard, A.L. (1982). J. Colloid Interface Sci. 2:508-520.
- Ravenhall, D.G., Forney, L.J., and Jazayeri, M. (1978). J. Colloid Interface Sci. 1:108-117.
- Solomon, P., Moyers, J., and Fletcher, R. (1983). Aerosol Sci. Technol., 2:455-464.
- Wang, H.C., and John, W. (1987). Aerosol Sci. Technol. 6:191-198.
- Wu, J.J., Cooper, D.W., and Miller, R.J. (1989). J. Environ. Sci. 4:52-56.

## BIOGRAPHICAL SKETCH

HungMin Chein was born in Kaoushiung, Taiwan, Republic of China, on November 26, 1963. He attended primary and secondary school in Kaoushiung. He received a Bachelor of Science degree in civil engineering from the National Taiwan University in July of 1986. After two-year of service in the military and one year working as a research assistant in the National Taiwan University, he decided to pursue graduate study in the United States. He became a graduate student in the Department of Environmental Engineering Sciences of University of Florida in January, 1990. He was awarded the Master of Engineering degree in May, 1992 and stayed on for his Ph.D degree in the air pollution program.

During the graduate study, his research work involved the following: (a) designed a modified virtual impactor with interchangeable nozzles to generate aerosols with narrow size distributions (Master's thesis); (b) designed a high-output, size-selective aerosol generator (Ph.D dissertation) for use in a new U.S. EPA human exposure laboratory; (c) combined data from an EAA, DMPS, and APS to obtain aerosol mass distribution parameters; (d) developed a submicron aerosol generator for EPA's human exposure laboratory; (e) evaluated two aerodynamic particle sizing devices (Aerosizer vs. APS); (f) conducted field tests of a military M-1 tank engine exhaust including comparison of an in-stack diffusion classifier with an in-stack low pressure impactor; (g) performed

experimental evaluations of an aerosol dilutor designed for use in high flow rate; (h) conducted field stack sampling tests for a battery production plant located in Tampa, Florida.

He was a teaching assistant in the course, Air Pollution Control Design (ENV 6126), in the spring semester, 1991. He co-taught Air Pollution Control Design (ENV 6126) and Atmospheric Dispersion Modeling (ENV 6146) with Professor Eric Allen in 1993. He also assisted his advisor, Professor Dale Lundgren, in instruction of several EPA short courses involving Particulate Emission Control, Method 5, and PM-10 stationary source sampling.

Following his final oral exam, he will receive his Ph.D degree in August, 1994. He is a member of the American Association for Aerosol Research, Air and Waste Management Association; American Conference of Governmental Industrial Hygienists; Inc.; Chinese Association for Aerosol Research; and Tau Beta Pi engineering honor society. He is married with Ma-Li Kuo and has a two-year-old daughter, Karen. After he receives the Ph.D degree, he plans to return to Taiwan and serve his own country.



I certify that I have read this study and that in my opinion it conforms to acceptable standards of scholarly presentation and is fully adequate, in scope and quality, as a dissertation for the degree of Doctor of Philosophy.



Dale A. Lundgren, Chairman  
Professor of Environmental  
Engineering Sciences

I certify that I have read this study and that in my opinion it conforms to acceptable standards of scholarly presentation and is fully adequate, in scope and quality, as a dissertation for the degree of Doctor of Philosophy.



Eric R. Allen  
Professor of Environmental  
Engineering Sciences

I certify that I have read this study and that in my opinion it conforms to acceptable standards of scholarly presentation and is fully adequate, in scope and quality, as a dissertation for the degree of Doctor of Philosophy.



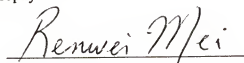
Paul A. Chadik  
Assistant Professor of Environmental  
Engineering Sciences

I certify that I have read this study and that in my opinion it conforms to acceptable standards of scholarly presentation and is fully adequate, in scope and quality, as a dissertation for the degree of Doctor of Philosophy.



Chen-Chi Hsu  
Professor of Aerospace Engineering,  
Mechanics & Engineering Science



I certify that I have read this study and that in my opinion it conforms to acceptable standards of scholarly presentation and is fully adequate, in scope and quality, as a dissertation for the degree of Doctor of Philosophy.



Renwei Mei  
Assistant Professor of Aerospace  
Engineering, Mechanics &  
Engineering Science

This dissertation was submitted to the Graduate Faculty of the College of Engineering and to the Graduate School and was accepted as partial fulfillment of the requirements for the degree of Doctor of Philosophy.

August 1994

  
Winfred M. Phillips  
Dean, College of Engineering  
Karen A. Holbrook  
Dean, Graduate School